The four-stage evolution of Martian mantle inferred from numerical simulation of the magmatism-mantle upwelling feedback

Masaki Ogawa

Department of Earth Sciences and Astronomy, University of Tokyo at Komaba,

Meguro, Tokyo, 153-8902, Japan

Phone: +81-3-5454-6612

e-mail: maogawa@g.ecc.u-tokyo.ac.jp

Key points

Two types of positive feedback have operated between magmatism and mantle upwelling flow in Mars to let its mantle evolve in four stages.

An initial extensive magmatism in the 1'st stage compositionally stratified the mantle to make it dormant in the 2'nd stage.

Episodic plume magmatism took place to stir the mantle and to release water from the interior of Mars in the 3'rd stage.

Abstract

To understand the overall features of the history of magmatic activities and surface environment on Mars, I used a numerical model of magmatism in the convecting mantle that is nominally anhydrous and internally heated. Magmatism occurs as an upward permeable flow of basaltic magma generated by decompression melting through matrix. The modeled mantle evolves in four stages. In Stage I, high initial temperature in the uppermost mantle causes an extensive magmatism intensified by two types of positive feedback that operate between magmatism and mantle upwelling flow, the MMUb and MMUc feedback: the buoyancy and volume change of matrix, respectively, caused by migrating magma that a mantle upwelling flow generates intensify the flow itself to generate more magma. The stratification suppresses mantle convection and magmatism for the next tens to hundreds of millions of years, allowing heat to build up in the mantle by internal heating (Stage II). Eventually, magma is generated at depth, and the MMUb feedback operates to cause an episodic plume magmatism that releases water from the interior of Mars (Stage III). The plume magmatism also stirs the mantle to make it more homogeneous and extracts heat producing elements from the deep mantle to let the magmatism itself wane and cease. In the final stage IV, mantle convection becomes more like a thermal convection. The episodic magmatism and water outgassing in Stage III account for the magmatism and clement surface environment observed for early Mars.

Plain language summary

Upwelling flow in the convecting mantle of a rocky planet causes magmatism, i.e., generates magma that migrates upward to the surface, when its interior is sufficiently hot. The numerical experiments presented here suggest that magmatism has intensified the mantle upwelling flow that caused the magmatism itself in Mars, and that its mantle has evolved in four stages due to this positive feedback: in Stage I, an extensive magmatism formed the crust and compositionally differentiated the mantle; in Stage II, the resulting compositional stratification of the mantle suppressed magmatism and mantle convection for tens to hundreds of millions of years to allow heat to build up in the deep mantle; in Stage III, magma was generated at depth, and the buoyancy of generated magma induced plumes that ascend through the stratified mantle to cause an episodic magmatism and water outgassing from the interior of Mars; in Stage IV, the magmatism and outgassing subsided due to extraction of heat producing elements from the mantle by the magmatism itself. The episodic magmatism and water outgassing in Stage III account for the magmatism and clement surface environment observed for early Mars.

Key words: 8121 Dynamics: convection currents and mantle plumes;

5455 origin and evolution;

8450 planetary volcanism;

Mars

1. Introduction

Understanding the history of Mars is a longstanding issue in studies of mantle dynamics in planets. In Mars, the crust was formed by 20-60 Myr since the solar system formation [*Kruijer et al.,* 2017, 2020], and an intrinsic magnetic field was induced until about 4 Gyr ago [*Acuna et al.,* 1999; *Lillis et al.,* 2013; *Vervelidou et al.,* 2017]. Then, magmatic activities took place in the Tharsis and other regions in the Noachian to early Hesperian [e.g., Greeley and Schneid, 1991; *Head et al.,* 2002; *Werner*, 2009; *Carr and Head,* 2010]. The surface environment was clement at that time [e.g., *Di Achille and Hynek*, 2010; *Fassett and Head,* 2011; *Ehlmann et al.,* 2011; *Mouginot et al.,* 2012], and its close link with magmatic activities is suggested from both observational and modeling studies [e.g., *Phillips et al.*, 2001; *Grott et al.,* 2011; *Morschhauser et al.,* 2011; *Halvevy and Head,* 2014; *Bouley et al.,* 2016; *Citron et al.*, 2018; *Wordsworth et al.,* 2021]. However, the magmatism waned, and the surface became colder and more arid since the late Hesperian, around 3 Gyr ago [e.g., *Carr and Head,* 2010; *Grott et al.,* 2013; *Ehlmann et al.,* 2016]. To clarify the physical processes through which these features arose in Martian history, I extensively analyzed the dynamics of magmatism in the convecting mantle, using the numerical model developed in *Ogawa and Yanagisawa* [2012] (called Paper 1 hereinafter).

Various numerical models of mantle evolution have been advanced to understand the history of Mars. Many studies that are based on parameterized models of

mantle convection have focused on clarifying the thermal history of Mars' interior and have suggested that the magnetic field, magmatism, and clement surface environment declined with time owing to cooling of the interior [*Nimmo and Stevenson*, 2000; *Hauck and Phillips,* 2002; *Breuer and Spohn*, 2003; *Fraeman and Korenaga,* 2010; *Morschhauser et al.,* 2011; *Grott et al.,* 2011; *Sandu and Kiefer*, 2012; *Samuel et al.,* 2021]. This view is maintained in two-dimensional annular models and three-dimensional spherical models of mantle convection, too [*Ruedas et al.,* 2013a,b; *Sekhar and King*, 2014; *Plesa et al.,* 2015, 2016, 2018]. Thermal history is, however, only one aspect of evolution of the mantle; evolution of compositional structure of the mantle is another important aspect. *Elkins-Tanton et al.* [2005] suggest that the magma ocean compositionally stratified the mantle at the beginning of Martian history. The stratified structure, however, survives convective stirring for billions of years and lets magmatism decline and cease within the first 1 Gyr or less of the calculated history of the mantle in numerical models published later [*Zaranek and Parmentier*, 2004; *Tosi et al.,* 2013; *Plesa et al.,* 2014; *Scheinberg et al.,* 2014]; this decline is too early to account for the observed history of Martian magmatism. A deeper understanding of mantle dynamics is called for to clarify the thermal and structural evolution of the mantle that exerts control over the history of magmatism, magnetic field, and surface environment in Mars.

To elucidate the nature of mantle dynamics in Mars, here, I use the numerical model developed in Paper 1 where the calculated history of magmatism and water outgassing broadly fits in with the observed history summarized above. The point of this model is that magmatism occurs as an upward permeable flow of basaltic magma generated by decompression melting through the convecting mantle. Later analyses [*Ogawa,* 2018, 2020] show that two types of positive feedback operate between thus modeled magmatism and mantle convection to play a key role in the dynamics of the mantle, depending on mantle viscosity and other model parameters. (See Section 3.2 below for more about the feedback.) The feedback can, indeed, cause magmatism and mantle convection even in a compositionally stratified mantle where thermal buoyancy alone cannot drive convection. Before the detailed analyses of *Ogawa* [2018, 2020], however, it was not possible to fully recognize the roles that the feedback plays in the mantle evolution model of Paper 1 and to predict with confidence how the mantle would have evolved in Mars under the control of the feedback. Besides, the control of evolution of the mantle, especially its structural evolution, over the surface environment and core dynamo of Mars has not been fully discussed in Paper 1. Here, I address these issues by more systematically carrying out numerical simulation of the feedback in wider range of model parameters.

2. Model description

A finite difference numerical code calculates the energy, mass, and momentum equations for magmatism and mantle convection that occur in a two-dimensional rectangular box under the Boussinesq approximation. (See Appendix A for the basic equations). The aspect ratio of the box is 4 with the depth of $d = 1000\ km$,

the ratio of volume to surface area of Martian mantle. Mantle materials are nominally anhydrous and contain incompatible heat producing elements (HPEs) that decay with time. The solidus temperature depends on water-content as well as depth. The rheology of solid mantle materials is Newtonian. The viscosity depends on temperature, depth, and water-content. Magmatism occurs as generation of basaltic magma by decompression melting and upward permeable flow of the generated magma through matrix. Water concentrates to magma in partially molten regions and is outgassed from the box, when it is transported upward to the topmost 10 km of the box by migrating magma. Magmatism induces a compositional heterogeneity in the mantle, which is transported by mantle convection. All the boundaries are shear stress free, and there is no mass flux of matrix and magma through the boundaries. The temperature is fixed at 250 K on the surface boundary, while the sidewalls are insulating. The box is placed on top of a heat bath of uniform temperature that is a model of the core. Its heat capacity is 18% of that of the mantle, as estimated from the mass of the core [e.g., *Yoshizaki and McDonough*, 2020].

2.1. The properties of convecting materials

The convecting material is a binary eutectic system. The composition is written as $A_\xi B_{1-\xi}$ where A stands for olivine and B stands for a mixture of garnet and pyroxene. The average composition in the box is $A_{0.64}B_{0.36}$ and corresponds to that of the mantle [e.g, *Yoshizaki & McDonough,* 2020], while the eutectic composition is $A_{0.1}B_{0.9}$ and corresponds to the basaltic composition. I assume that the end-member B transforms into its crustal phase at depths less than d_{BE} to model the basalt-eclogite (BE) transition. (See Table 1 for the values of constants.)

The density of solid materials ρ_s depends on its temperature T and composition ξ_s as

$$\rho_s = \rho_0 \left[1 - \alpha T + \beta_s \left(1 - \xi_s\right)\right]. \quad (1)$$

Here, ρ_0 is the reference density, α the thermal expansivity, and β_s a constant defined as

$$\beta_s = \begin{cases} 0.067 & if\ d - z > d_{\mathrm{BE}} \\ -0.17 & if\ d - z \leq d_{\mathrm{BE}} \end{cases}, \quad (2)$$

where z is the height measured from the core-mantle boundary (CMB). The positive value of β_s at $d - z > d_{\mathrm{BE}}$ implies that basaltic materials $A_{0.1}B_{0.9}$ are denser than the average mantle material $A_{0.64}B_{0.36}$ in the mantle. The value of β_s is determined from the density contrast between the average mantle materials and basaltic materials, around 120 kg m^{-3} [e.g., *Irifune and Ringwood,* 1993]. Above the BE boundary ($d - z \leq d_{\mathrm{BE}}$), however, β_s is negative, implying that basaltic materials are buoyant.

The density of melt ρ_l depends on T, z, and ξ_l (the composition of melt) as

$$\rho_l = \rho_0 \left\{1 - \alpha T + \beta_l \left(1 - \xi_l\right) - \Delta_l \left[1 + \beta_l \left(1 - \xi_l\right)\right]\right\}, \quad (3)$$

where

$$\Delta_l = \Delta_l^0 \left[1 + (d-z)/\lambda_\infty\right]^{-2} \quad (4)$$

expresses density reduction by melting. (See *Ogawa* [2018] for the derivation of Equation (3).) The values of Δ_l^0 and λ_∞ in Table 1 are estimated from the solidus curve discussed below through the Clausius-Clapeyron relationship. Equations (1) to (4) with the values of constants listed in Table 1 imply that a basaltic melt with $\xi_l = 0.1$ is less dense than the average solid material with $\xi_s = 0.64$ at all depths, as illustrated in Figure 1a. The density inversion between solid mantle materials and basaltic magma in the deep mantle [e.g., *Sanloup et al.,* 2013] is not taken into account. Melting at such a great depth is not common in the models presented below, and it is safe to neglect the density inversion.

The viscosity depends on T, z, and the water-content ϕ_w as

$$\eta = \eta_0 \exp\left[\, \mathrm{E}\,(T_{\mathrm{ref}} - T) + V_p(d-z)/d - V_w\phi_w/\phi_{w0}\right] \quad (5)$$

where ϕ_{w0} and T_{ref} are constants. Other parameters including the reference viscosity η_0 are free parameters, and their values are given in Tables 2 and 3. The default value of E shown in Table 2 implies that a temperature-variation of 100 K causes a viscosity-variation of a factor 3, an appropriate value to mimic a thermal convection of mantle materials with power law rheology by that with Newtonian rheology [e.g., *Dumoulin et al.*, 1999].

The solidus temperature T_s depends on depth and water-content as

$$T_s = T_s^0\,(\phi_w)\,(1+G) \quad (6)$$

where

$$G = \tfrac{1}{\rho_0 \Delta h} \int_0^P \Delta_l \ \mathrm{dP} \quad (7)$$

and

$$T_s^0\,(\phi_w) = \ T_s^0 - \Delta T_s \min\left(1, \tfrac{\phi_w}{\phi_{w0}}\right), \quad (8)$$

(see Figure 1b). Here, Δh is the latent heat of melting at $z = 0$, $P = \rho_0 g(d-z)$ is the lithostatic pressure, g is gravitational acceleration, and the solidus-reduction by water is truncated at $\phi_{w0} = 1000\ ppm$. ϕ_w is almost always less than ϕ_{w0} in the mantle calculated here, and this truncation does not influence the numerical results. The values of the constants in Equations (4) and (6)-(8) presented in Tables 1 and 2 are estimated from the dry and wet solidus of mantle materials [*Litasov et al.,* 2014].

2.2. The initial condition

The initial thermo-chemical state of the mantle is specified by the initial distributions of "reduced" enthalpy h, bulk composition ξ_b, internal heating rate Q, and water-content ϕ_w together with the initial temperature of the core. Here, the reduced enthalpy $h = H - P/\rho_0$ is defined as

$h = C_p T + \Delta \mathrm{h} \ \ (1 + G)$ (9)

where H is the enthalpy, C_p is the specific heat, and ϕ is the melt-content, while

$\xi_b = \phi \xi_l + (1 - \phi) \xi_s.$ (10)

The initial distribution of h is

$h = C_p T^{\mathrm{eq}}$ (11)

where "the equivalent temperature" T^{eq} is illustrated in Figure 1b; T_{is} in the figure is in the range of [1800 K, 2400 K], while T_{ib} in the range of [1000 K, 1800 K]. I assume that $T_{\mathrm{is}} > T_{\mathrm{ib}}$ holds, motivated by earlier models of the "mantle overturn" that is expected to have occurred just after the planetary formation owing to a gravitational instability of the mantle differentiated by the magma ocean [e.g., *Elkins-Tanton et al.,* 2005]. I also assume that the initial temperature of the core T_{ic} is equal to T_{is} in most cases and hence that $T_{\mathrm{ic}} > T_{\mathrm{ib}}$, following *Elkins-Tanton et al.* [2005]; the excess temperature of the core with respect to the deep mantle is necessary to keep the heat flow on the CMB high enough to drive core-dynamo for several hundred million years in the early mantle [*Nimmo and Stevenson*, 2000; *Breuer and Spohn*, 2003]. Random noise is added to the initial T^{eq}-distribution to start convection, unless otherwise mentioned.

The initial distributions of ξ_b, Q, and ϕ_w are uniform. Their values are $\xi_b = \xi_{\mathrm{init}} = 0.64$, $Q = Q_0 + \Delta Q$ (see Table 1), and $\phi_w = \phi_w^{\mathrm{init}}$ (see Table 3). I did not take account of the compositional stratification of the mantle that is suggested to have been induced in Mars by the magma ocean and mantle overturn [e.g, *Elkins-Tanton et al.,* 2005; *Scheinberg et al.,* 2014; *Maurice et al.,* 2017]. Although the influence of initial mantle stratification on later mantle evolution is an important issue addressed in the literature [*Tosi et al.,* 2013; *Plesa et al.,* 2014; *Scheinberg et al.,* 2014; *Samuel et al.,* 2021], here, I concentrate on exploring how the dynamics of magmatism and mantle convection controls mantle evolution; I will further discuss the influence of initial mantle structure later in Section 4.1.

I carried out numerical experiments at various values of the Rayleigh number Ra defined by Equation (A3) of Appendix A, the reference permeability Pm defined by Equation (A6), T_{ib} illustrated in Figure 1b, and the initial water-content ϕ_w^{init}, as listed in Table 3. Here, Ra is inversely proportional to the reference viscosity η_0 and expresses how easily mantle convection takes place. The range of its value in the table, 3×10^5 to 3×10^6, corresponds to that of η_0 of 10^{20} to 10^{21} Pa s. On the other hand, Pm expresses how easily magma migrates in partially molten regions. This parameter controls the mechanical coupling between magmatism and mantle convection, as I will discuss in detail in the next section. I also varied the values of other parameters listed in Table 2 to see how the numerical results depend on the mechanical and thermodynamic properties of mantle materials.

3. Results

3.1. The reference case

Figures 2 to 5 show the reference model of Case H16-050. The assumed values of the free parameters are: the Rayleigh number $Ra = 3.2 \times 10^6$, corresponding to $\eta_0 = 10^{20}$ Pa s; $T_{\rm ib} = 1600$ K (see Figure 1b); the initial water-content $\phi_w^{\rm init} = 500$ ppm; the reference permeability Pm = 3.2.

3.1.1. The four stages of mantle evolution

Figures 2 and 3 as well as the animation in Supplement show that the mantle evolves in four stages. In Stage I (see Figures 2a-d for 0.001 Gyr), an extensive magmatism caused by high initial temperature forms the basaltic crust along the surface boundary and a layer of residual materials depleted in HPEs and water underneath. The residual layer is compositionally buoyant and stays in the uppermost mantle to suppress convection and magmatism for more than 100 Myr in the next Stage II (Figures 2a-e and 3c,e), allowing the temperature to rise in the deep mantle due to internal heating (Figures 2a,f). Eventually, hot and partially molten plumes are generated at depth, which ascend to the surface to cause magma-eruption, i.e., upward flux of magma across the basalt-eclogite phase boundary after 0.19 Gyr (Stage III in Figure 2a-e). This magmatism episodically outgasses water from the mantle (Figure 3d), thickens the crust (Figure 3f and Δd in Table 3), and concentrates HPEs in the box to the crust (Figures 2c for 0.629 Gyr and 3g). The plumes also stir the mantle to dissolve the bulk of the compositional stratification formed in Stage I, although the recycled crustal materials on the CMB survives the stirring (Figure 2b). As the mantle becomes more depleted in HPEs, however, the mid mantle becomes colder (Figure 2f), and the plume magmatism wanes and eventually ceases at 2.75 Gyr (see Figures 2e and 3c). After that (Stage IV), mantle convection driven by thermal buoyancy further stirs the mantle to make it more homogeneous as shown in Figures 2b-d.

3.1.2. The secondary magmatism and crustal recycling in Stage I

In Figure 4, I delineate the extensive magmatism in Stage I in more detail. At 0.001 Gyr, basaltic magma generated by the high initial temperature migrates upward to the surface and forms the "primary" crust, leaving residual materials behind in the uppermost mantle. Before this primary magmatism ceases, however, mantle convection starts to cause the "secondary magmatism" (see Figure 4a for 0.004 and 0.01 Gyr). The crust newly generated by the secondary magmatism pushes the primary crust aside, a large fraction of which sinks to the CMB and accumulates there (Figure 4b).

The driving mechanism of the secondary magmatism is a positive feedback that operates between magmatism and mantle upwelling flow, as indicated in Figure 4c. Here, I decomposed the convective velocity of matrix $\mathbf{U}$ calculated at 0.01 Gyr into three components: the one driven by thermal and compositional buoyancy $\mathbf{U}^{\rm TC}$; that by melt-buoyancy $\mathbf{U}^{\rm melt}$; that by volume change of matrix caused by upward migration of magma $\mathbf{U}^{\rm dv}$. (See Appendix B for the definition of these components.) The overall flow $\mathbf{U}$ points upward to generate magma

beneath the black bars in Figures 4a,c. However, $\mathbf{U}^{\mathrm{TC}}$ points downward there, because the head of the upwelling materials beneath the black bar has $\xi \approx 0.64$ (see the arrow in Figure 4b) and is compositionally denser than the adjacent residual layer where $\xi \approx 0.9$. $\mathbf{U}$ points upward there, because $\mathbf{U}^{\mathrm{melt}}$ and $\mathbf{U}^{\mathrm{dv}}$ point upward, and the sum of these two components surpasses the opposing flow $\mathbf{U}^{\mathrm{TC}}$. Namely, buoyancy and upward migration of magma that is generated by a mantle upwelling flow drive the upwelling flow itself. I will call this positive feedback as the magmatism-mantle upwelling (MMU) feedback and will further discuss it below. (See also Appendix B.)

The crustal recycling caused by the secondary magmatism lets the average heat flow on the CMB h_{fCMB} rapidly decline with time in Stage I, as observed in Figure 3b. At the beginning of the calculation, the excess temperature of the core with respect to the deep mantle assumed in the initial condition induces hot ascending plumes that extract heat from the core (Figure 4a for 0.010 Gyr). The plumes are, however, soon shut off by the recycled crustal materials (Figure 4a for 0.015 Gyr). Besides, the crustal materials are enriched in HPEs and raises the temperature at the base of the mantle, reducing the temperature contrast across the CMB (Figure 4a for 0.181 Gyr and the purple curve in Figure 2f). Consequently, h_{fCMB} declines below the lower limit necessary to drive core-dynamo, around 10 $mW\ m^{-2}$ [*Silber et al.,* 2019; *Gilfoy and Li,* 2020], within 58 Myr (see t^{10}_{CMB} in Table 3).

3.1.3. The MMUb feedback and the plume-magmatism in Stage III

The MMU feedback is the cause of the episodic magmatism in Stage III, too, as shown in Figure 5 where the convective flow at 0.629 Gyr is analyzed. A mantle upwelling flow generates magma beneath the black bar in the figure. This upwelling flow is driven by the buoyancy of the magma itself: $\mathbf{U}$ points upward in spite of the opposing flow $\mathbf{U}^{\mathrm{TC}}$ there, because $\mathbf{U}^{\mathrm{melt}}$ points upward. The contribution of $\mathbf{U}^{\mathrm{dv}}$ to $\mathbf{U}$ is negligible, because the partially molten region is mostly beneath the lithosphere and does not extend to the surface boundary, as further discussed in Appendix B. The MMU feedback that occurs through $\mathbf{U}^{\mathrm{melt}}$ will be denoted as the MMUb feedback, hereinafter.

3.1.4. Fixed location of plume magmatism

Figure 2e shows that plume magmatism repeatedly occurs at fixed locations in Stage III. Figure 2c for 1.505 Gyr show how this feature arises. The crust is particularly enriched in HPEs beneath the bars at the top of the figure. This crustal enrichment makes the lithosphere there locally thinner than the average and allows magmatism to occur (Figure 2a). The magmatism adds more HPEs to the crust, making these portions of the lithosphere even thinner. I found that this tendency is more prominent at higher sensitivity of viscosity to temperature E (Cases H14-025, H14-050b, H16-050h in Table 3).

3.2. The MMU feedback and the four-stage evolution

To more clearly show what roles the MMU feedback plays in the four-stage evo-

lution of the mantle discussed above, I further calculated the model at different values of the reference permeability Pm.

Figure 6 shows how the mantle evolves at a higher Pm of 32, 10 times as high as the value for the reference case (Case H16-050i). An extensive magmatism forms the crust and differentiates the mantle to compositionally stratify it in Stage I, as shown in Figure 6b for 0.002-0.022 Gyr. The mantle stratification is more prominent than that formed in the reference case (Figure 2b) and persists throughout the rest of the 4.5 Gyr calculated history. The persistent stratification suppresses magmatism after Stage I (Figures 6e,f), despite that the HPEs raise the temperature in the deep mantle and drive a thermal convection in the shallow mantle (Figure 6a for 2.946 Gyr). Namely, Stage III does not arise at higher Pm.

The mantle stratification of Case 16-050i is more prominent than that of the reference case, because the MMU feedback operates in a different way in Stage I owing to the higher Pm. The MMUb feedback does not operate, as can be seen from the negligibly small $\mathbf{U}^{\rm melt}$ in Figure 6c: magma in partially molten regions is drained upward to the surface too efficiently to drive $\mathbf{U}^{\rm melt}$. The efficient drainage of magma, however, causes a faster volume change of matrix to drive a mantle upwelling flow $\mathbf{U}^{\rm dv}$ that is about 10 times faster than that of the reference case (see Figure 4c) beneath the black bar shown in Figure 6c. This faster upwelling flow generates a larger volume of magma and residual materials to induce the more prominent mantle stratification; I will denote the MMU feedback that occurs through $\mathbf{U}^{\rm dv}$ as the MMUc feedback, hereinafter.

The mantle does not evolve in the four stages at a lower Pm of 0.32, 1/10 of the value for the reference case, too, as shown in Figure 7 (Case H16-050j). Because of the low Pm, $\mathbf{U}^{\rm dv}$ is negligible, and the MMUc feedback does not operate. Instead, the buoyancy of magma drives the upwelling flow that generates the magma (see $\mathbf{U}$ and $\mathbf{U}^{\rm melt}$ beneath the black bar in Figure 7c), implying that the MMUb feedback discussed in Section 3.1.3 is substantial. The convective flow driven by the MMUb feedback efficiently stirs the mantle, and the mantle becomes compositionally almost homogeneous by 0.595 Gyr despite the mantle differentiation caused by the initial extensive magmatism (see Figure 7b). Indeed, *Ogawa* [2018] shows that the mantle becomes more compositionally homogeneous after a magmatic event, as the MMUb feedback becomes more substantial. Since the mantle remains homogenous, Stage II when the mantle is dormant does not arise, and heat does not build up in the deep mantle. Therefore, Stage III does not arise, too; magmatism monotonously declines with time, as the mantle is cooled (Figures 7d,e). This magmatism does not outgas water except for the first 200 Myr (Figure 7f), because magma-ascent is so slow that magma solidifies by conductive cooling from the surface before reaching the topmost 10 km of the box where water outgassing is assumed to occur.

The parameter search illustrated in Figure 8 shows that the MMU feedback lets the mantle evolve in the four stages shown in Figure 2 only at "moderate" Pm indicated by the solid circles. At lower Pm, Stage II does not arise, since

the MMUb feedback stirs the mantle so efficiently that the mantle remains homogeneous in Stage I (Figure 7). The lower end of the range for "moderate" Pm decreases with decreasing $T_{\rm ib}$ and Ra, because the MMUb feedback becomes less active as the mantle becomes stiffer [*Ogawa*, 2018]. In contrast, Stage III does not arise at higher Pm, because the mantle stratification induced in Stage I by the MMUc feedback is so prominent as to totally suppress plume magmatism throughout the rest of the calculated history. The upper end of the range for moderate Pm does not noticeably depend on Ra and $T_{\rm ib}$, since the vigor of the MMUc feedback is determined by viscosity variation in the uppermost mantle rather than the viscosity itself (see Appendix B).

At a moderate value of $Pm = 3.2$, I also confirmed that the mantle evolves in the four stages regardless of the values of $T_{\rm is}$ and $T_{\rm ic}$ (see Figure 1b), the initial water-content $\phi_w^{\rm init}$, and the parameter values that characterize material properties E, V_p, V_w, and ΔT_s, as summarized in Table 3.

In Sections 3.3-3.5 below, I concentrate on the four-stage evolution of the mantle calculated at moderate Pm, since this type of mantle evolution is the most relevant to Mars, as will be discussed in Section 4.

3.3. Crustal recycling and the heat flux on the CMB in Stage I

In the reference case, the heat flow on the CMB $h_{\rm fCMB}$ rapidly declines with time in Stage I, because a part of the crustal materials generated by the initial extensive magmatism recycle into the deep mantle to internally heat it and also to shut off hot plumes ascending from the CMB (see Section 3.1.2). To see how this decline in $h_{\rm fCMB}$ depends on the model parameters, I present $t_{\rm CMB}^{10}$, the time when $h_{\rm fCMB}$ declines below 10 $mW\ m^{-2}$, for all the cases in Table 3. I also present a plot of $t_{\rm CMB}^{10}$ against the initial temperature at the base of the mantle $T_{\rm ib}$ (see Figure 1b) for selected cases in Figure 9a. The decay time $t_{\rm CMB}^{10}$ is around 100 Myr or less at $T_{\rm ib} \geq 1400\ K$. The short $t_{\rm CMB}^{10}$ is a consequence of the large volume of recycled crustal materials (see Figure 9c). At lower $T_{\rm ib}$, however, the volume of recycled crustal materials becomes smaller, their effects on $h_{\rm fCMB}$ becomes limited, and $t_{\rm CMB}^{10}$ becomes as long as 200-300 Myr at $T_{\rm ib} = 1000\ K$ (see Figure 9a).

3.4. The plume-magmatism in Stage III

The plume magmatism caused in Stage III by the MMUb feedback is important for understanding early Mars, and I studied it in more detail. I found that the total amount of crustal growth Δd and that of water-outgassing Δl due to the plume magmatism increase with increasing Rayleigh number Ra, as shown in Figures 10a,b (see also Table 3). This trend arises, since the MMUb feedback is more substantial at higher Ra (see Appendix B). The average outgassing rate defined by

$$\overline{w} = \Delta l \left(t_{\rm GAS}^{e} - t_{\rm GAS}^{b} \right)^{-1}, \quad (12)$$

is, however, 10^{-4}-10^{-3} mm yr^{-1} and does not correlate with Ra in Figure 10c,

when $Ra > 1 \times 10^6$. (Here, $t^b_{\rm GAS}$ and $t^e_{\rm GAS}$ are the time when outgassing begins and ends, respectively. Note that $\overline{w} = 0$ holds in many of the cases calculated at $Ra = 3.2 \times 10^5$, as shown in Table 3, and that these cases are not included in Figure 10c.) Plume magmatism that outgasses water in Stage III is a stochastic process, and the resulting dispersion of $\overline{w}$ overshadows the possible dependence of $\overline{w}$ on Ra. I also found from Table 3 that the dependences of Δd and Δl on the parameters that characterize material properties E, V_w, V_p, and ΔT_s are not so strong as to undermine the overall trends observed in Figure 10.

3.5. The crust

It is important to see how thick the crust is and how the thickness is determined in the model, too. The calculated thickness of the crust is mostly 70-90 km at 4.5 Gyr and does not show clear dependence on Ra, $T_{\rm ib}$ and other parameters (see $d^e_{\rm crst}$ in Table 3). This feature arises, because the thickness of the basaltic crust is limited by the depth of the basalt-eclogite phase boundary rather than by mantle dynamics: when the base of the crust generated by the magmatism of Stages I and III becomes deeper than the phase boundary, the spilled basaltic materials recycle into the mantle (see Figure 9c).

I also found that the crustal fraction of HPEs at the beginning of Stage III increases from around 0.25 to around 0.4 as $T_{\rm ib}$ increases from 1000 K to 1800 K (see $q^b_{\rm crst}$ in Table 3). However, the crustal fraction is mostly in the range of 0.3 to 0.6 and does not show clear correlation with $T_{\rm ib}$ and other model parameters at the end of Stage III (see $q^e_{\rm crst}$ in the table); $q^e_{\rm crst}$ only weakly correlates with the Rayleigh number Ra (0.3-0.45 at $Ra = 3.2 \times 10^5$ to 0.4-0.6 at $Ra = 3.2 \times 10^6$). This feature of $q^e_{\rm crst}$ arises, because magmatism continues to extract HPEs from the mantle, until the mantle becomes too depleted in HPEs to sustain the magmatism.

4. Discussion

In Figure 11, I present an illustration of the four-stage evolution (FSE) model of Martian mantle that I obtained from the numerical experiments discussed above. An extensive magmatism forms the crust and compositionally stratifies the mantle at the beginning of the history of the mantle (Stage I). This magmatism occurs as an upward segregation of magma generated by high initial temperature followed by the secondary one that the combined MMUb and MMUc feedback causes: the buoyancy and upward migration, respectively, of magma generated by a mantle upwelling flow intensify the upwelling flow itself to generate more magma. The compositionally stratified mantle becomes dormant for the next tens to hundreds of millions of years, and heat builds up at depth by internal heating (Stage II). Eventually, partially molten plumes develop in the deep mantle and ascend to the surface by the MMUb feedback to cause an episodic magmatism and outgassing (Stage III). These plumes also stir the mantle to dissolve its stratified structure formed in Stage I. The plume magmatism, however, declines and ceases, as the magmatism extracts HPEs from the mantle, and thermal buoyancy becomes the main driving force of mantle

convection in the final Stage IV.

4.1. The evolution of mantle structure

The four stages of the FSE model arise, because an extensive magmatism makes the mantle compositionally stratified at the beginning of the calculated history, and the MMUb feedback stirs the mantle to dissolve the stratified structure later. The model is, therefore, fundamentally different from many of earlier parameterized and three-dimensional models of mantle evolution where the structure of mantle remains unchanged, mostly homogeneous, throughout its history and the mantle evolves solely by its cooling [*Nimmo and Stevenson*, 2000; *Hauck and Phillips,* 2002; *Breuer and Spohn*, 2003; *Fraeman and Korenaga,* 2010; *Morschhauser et al.,* 2011; *Grott et al.,* 2011; *Sandu and Kiefer*, 2012; *Sekhar and King,* 2014; *Plesa et al.,* 2015, 2016, 2018; *Samuel et al.,* 2021]. The magmatism predicted from these models is active at the beginning of the evolutionary history and monotonously declines with time, as the mantle is cooled (see *Grott et al.* [2013] for a review). A similar evolution is observed in Case H16-050j calculated at low Pm where convection driven by the MMUb feedback efficiently stirs the mantle to keep it almost homogeneous throughout the calculated evolutionary history despite mantle differentiation caused by the magmatism of Stage I (Figure 7); the dormant Stage II and reactivation of magmatism in Stage III do not occur in this case. (See also *Reudas et al.* [2013a,b].) The structural evolution of the mantle that is caused by the initial extensive magmatism and the later MMUb feedback is the essence of the FSE model.

The crucial role that the MMUb feedback plays in the FSE model becomes clearer, when the model is compared with earlier models of evolution of the mantle that is compositionally differentiated at the beginning of its history by the magma ocean and subsequent mantle overturn [*Zaranek and Parmentier*, 2004; *Elkins-Tanton et al.,* 2005; *Tosi et al.,* 2013; *Plesa et al.,* 2014]. The stratified structure of the mantle formed by the differentiation survives later convective stirring driven by thermal buoyancy for billions of years because of the large density contrast that accompanies the structure [e.g. *Zaranek and Parmentier*, 2004]. The MMUb feedback can, however, more effectively dissolve such a stratified structure of the mantle (see Figures 2 and 5), because melt-buoyancy that drives the feedback is much stronger than thermal buoyancy.

Despite the evolution of mantle structure caused by the MMUb feedback, some quantitative aspects of the FSE model are similar to those of earlier thermal history models in the literature. In Figure 3a, the average temperature in the convecting box decreases by about 200 K over the past 4 Gyr. This temperature decrease is comparable to those predicted in the nominal models of *Hauck and Phillips* [2002] (see their Figure 2) and *Morschhauser et al.* [2011] (see their Figure 8). The fraction of water in the mantle that survives outgassing by magmatism until today is 0.25-0.65 for the FSE model calculated at $Pm = 3.2$. (The fraction can be estimated from Table 3 as $\phi_w^m/\phi_W^{\rm init}$.) This range of fraction is close to that estimated earlier, 0.2-0.6, from parameterized thermal history models by *Morschhauser et al.* [2011] (see their Figures 2 and 8), although is

lower than 0.9-0.95 estimated by *Hauck and Phillips* [2002] (see their Figure 11). The crustal thickness of 70-90 km today in the FSE model (see $d^e_{\rm crst}$ in Table 3) is greater than 30-80 km predicted by *Morschhauser et al.* [2011] (see their Figure 3) but is within the range of 20-230 km predicted by *Hauck and Phillips* [2002] (see their Figures 3-12); I will further discuss the crustal thickness in the next Section. Given the fundamental difference in the way mantle evolves between the FSE model and the earlier thermal history models, however, the significance of the quantitative similarities is not clear.

To further develop the FSE model, it is important to take account of the effects of "initial mantle differentiation" caused by the magma ocean and mantle overturn [*Elkins-Tanton et al.,* 2005; *Scheinberg et al.,* 2014; *Maurice et al.,* 2017]. At moderate Pm at which the FSE model holds in the present calculation (see Figure 8), the initial mantle differentiation may induce a compositionally stratified structure that is gravitationally too stable even for the MMUb feedback to dissolve later; Stage III would not arise in this case. At lower Pm at which the mantle remains compositionally homogeneous in the present calculation (see Figure 7), on the other hand, the initial mantle differentiation may induce a stratified structure in Stage I and hence may let the mantle evolve in the four stages illustrated in Figure 11. To what extent the magma ocean and mantle overturn differentiates the mantle is, however, a delicate issue [*Scheinberg et al.,* 2014; *Maurice et al.,* 2017; *Ballmer et al.,* 2017; *Boukare and Ricard,* 2017; *Boukare et al.,* 2018], and unified treatments of mantle evolution from the era of the magma ocean until today are necessary to ultimately understand the history of Mars. (I will return to the issue of early mantle differentiation in Mars in Section 4.2, below.) An extension of the model to three-dimensional (3D) space [*Keller and Tackley,*2009; *Sramek and Zhong*, 2012; *Sekhar and King,* 2014; *Plesa et al.,* 2015, 2016, 2018] is also important for more quantitative estimates of magmatism and outgassing on Mars. Hot upwelling flows are implicitly assumed to be sheet-like in 2D models, while they can be cylindrical in 3D space. Because of this difference in the geometry of upwelling flows, 2D models tend to overestimate the rate of magma-generation and outgassing.

4.2. Implications for Mars

Among the models calculated at various reference permeability Pm, the FSE model calculated at moderate Pm fits in with the observed history of Martian crust best. The plume magmatism of Stage III (see Figures 2 and 3) and its decline toward Stage IV account for the active magmatism in early Mars and its decline since the Hesperian [*Greeley and Schneid,* 1991; *Head et al.,* 2002; *Werner,* 2009; *Carr and Head,* 2010]. The history of the crust and recycled crustal materials on the CMB shown in Figure 2b and the animation in Supplement accounts for the fate of crustal materials in Mars inferred from isotopic studies of Martian meteorites [*Foley et al.,* 2005; *Debaille et al.,* 2009]: the crustal materials generated at the beginning of the 4.5 Gyr history are sequestered from the convecting mantle until today both in the model and in Mars. The models calculated at higher or lower Pm are, in contrast, at odds with the

observed features of Mars: no magmatic activity takes place after the crustal formation in Stage I in the models calculated at higher Pm (see Figure 6); most of the crustal materials formed in Stage I are recycled and mechanically stirred into the mantle later by convection at lower Pm (Figure 7).

The FSE model also accounts for the observed history of surface environment on early Mars. The episodic water-outgassing of Stage III shown in Figure 3d is consistent with the episodic occurrence of liquid water on the surface of early Mars [e.g., *Olsen and Rimstidt,* 2007; *Hoke et al.,* 2011]. The calculated rate of water-outgassing is probably high enough to bring a clement environment to Martian surface. Indeed, the average outgassing rate $\overline{w}$ shown in Figure 10c and Table 3 is 10^{-4}-10^{-3} *mm* yr^{-1}, which is equivalent to 3×10^4-3×10^5 *mol* s^{-1} on Mars, at the Rayleigh number Ra higher than 10^6. This water-outgassing rate corresponds to the hydrogen flux of 7×10^2- 1×10^5 mol s^{-1}, if the ratio of H_2 to H_2O is 0.025 to 0.65 in the outgassed "water" [*Ramirez et al.,* 2014; *Wordsworth et al.*, 2021]. The calculated range of hydrogen flux encompasses that necessary to episodically bring a clement environment to the surface of Mars (see Figure 2 of *Wordsworth et al.* [2021]), when the ratio r_m of peak outgassing rate to $\overline{w}$ is 10^2-10^3; this range of r_m overlaps with that for the FSE model (see Table 3). The shift of surface environment of Mars from a clement one to a colder and more arid one since the Hesperian [e.g., *Ehlmann et al.,* 2011] can be accounted for by the decline of outgassing from Stage III toward Stage IV.

It is more difficult to compare the FSE model with earlier estimates of surface and near-surface water inventory of Mars [e.g., *Car and Head,* 2003; *Wernicke and Jakosky,* 2021; *Scheller et al.,* 2021]. The average outgassing rate $\overline{w}$ of 10^{-4}-10^{-3} *mm* yr^{-1} and the total amount of water Δl outgassed in Stage III of 20-200 m at $Ra > 1 \times 10^6$ shown in Figures 10b,c are comparable to those suggested for early Mars from a numerical model of hydrological cycle of water [*Scheller et al.*, 2021]. The water-content in today's mantle ϕ_w^m of 100-200 ppm (see Table 3) and the above-mentioned range of Δl, which implies 6-60 ppm higher water-content at the beginning of Stage III, are acceptable as the value for Mars constrained from studies of Martian meteorites [*McCubbin et al.,* 2012]. Hydrological cycle of water on Martian surface is, however, a complicated process that depends on hydration of the crust and atmospheric escape, too [*Scheller et al.*, 2021]. Further studies based on the FSE model combined with models of hydrological water cycle on the surface are necessary to see if the model is compatible with the water inventory in Mars.

A testable prediction of the FSE model is Stage II when the mantle is dormant. This feature does not contradict with the observed history of Martian magmatism so far. After the crustal formation that occurred within 20-60 Myr since the solar system formation [*Dabaille et al.,* 2009; *Kruijer et al.,* 2020], magmatic activities that were as vigorous as the late-Noachian to early Hesperian one have not been reported for the pre-Noachian period [*Greely and Schneid,* 1991; *Grott et al.,* 2013]. The dormant Stage II is also a likely reason why the surface environment was not so clement on Mars in the early to middle Noachian as it

was in the late Noachian to early Hesperian [*Ehlmann et al.,* 2011]. Clarifying whether or not there was such a dormant era in the history of early Mars is a key for understanding the entire 4.5 Gyr evolutionary history of Mars.

The detail of Stage I delineated in Figure 4, on the other hand, is important for understanding the early differentiation of Martian mantle. Isotopic studies of Martian meteorites suggest that the crust of Mars was formed over a prolonged period of 10 Myr or more [*Debaille et al.,* 2009; *Kruijer et al.,* 2017, 2020]. This prolonged period is difficult to account for by simple cooling and solidification of the magma ocean and has been ascribed to crustal formation by mantle overturn or to the blanketing effect of a dense atmosphere (see the references above). The early differentiation of Stage I, however, takes as long as 15 Myr in Figure 4 because of the secondary magmatism caused by the combined MMUb and MMUc feedback. This long duration of the secondary magmatism can also account for the prolonged crustal formation in Mars.

In addition to the duration time, Stage I has an implication for the spatial extent of early mantle differentiation, too. Mars had an intrinsic magnetic field until as late as 4 Gyr ago [*Acuna et al.,* 1999; *Lillis et al.,* 2013; *Vervelidou et al.,* 2017]. Figure 9, however, suggests that the heat flow on the CMB could have remained high enough to drive core dynamo so long, only when the early mantle differentiation, including the one caused by the magma ocean and mantle overturn, was not so extensive as to form a thick layer of recycled crustal materials on the CMB. Future exploration of seismic structure of the deep mantle would be informative to further constrain the extent of early mantle differentiation in Mars, since such recycled materials are most likely to have survived convective stirring until today, as suggested from Figure 2b. (See also the animation in Supplement.)

The history of average surface heat flow $h_{f,srfc}$ over the past 4 Gyr shown in Figure 3b is broadly consistent with that of Mars $h^{\rm obs}_{f,srfc}$ estimated from the elastic thickness of the lithosphere [e.g., *Ruiz et al.,* 2011; *Broquet and Wieczorek,* 2019; *Ding et al.,* 2019]. The heat flow $h_{f,srfc}$ is typically 40-60 mW m^{-2} with occasional high spikes for the first 1.5 Gyr and then declines to 20-25 mW m^{-2} today. The spikes in Figure 3b and the lateral variation in the surface heat flow in Stages III and IV inferred from the temperature-distribution in the uppermost mantle (see Figure 2a), however, suggest that a detailed comparison of $h_{f,srfc}$ and $h^{\rm obs}_{f,srfc}$ may not be informative. Rather, lateral variation of the surface heat flow, and hence that of the thickness of the lithosphere, may be more important for understanding Mars. Magma-eruption tends to repeatedly occur at specific locations where the lithosphere is thinner than its average due to crustal enrichment in HPEs, as discussed in Section 3.1.4 (see Figure 2e). Similarly, HPE-enrichment in the crust may allow magmatism to take place at specific locations on Mars, too. Hot plumes that grow from specific sites in the deep mantle are not the only possible explanation for Martian magmatism that continues for billions of years in Tharsis and Elysium regions [e.g., *Keller and Tackley,* 2009; *Kiefer and Li,* 2009; *Sramek and Zhong,* 2012; *Sekhar and King,*

2014]. (See also *Schumacher and Breuer* [2007].)

Finally, a comment is necessary on the current thickness of the crust, 70-90 km, calculated in the model (see $d^e_{\rm crst}$ in Table 3). This thickness is greater than that in the southern hemisphere of today's Mars, around 60 km [*Zuber et al.,* 2000]. The crustal thickness at the beginning of Stage III, typically 60-70 km (see $d^b_{\rm crst}$), is also greater than that of pre-Noachian Mars inferred from isotopic studies of Martian meteorites [*Norman,* 1999]. The crustal thickness is, however, determined from the depth of the basalt-eclogite transition in the FSE model, as can be seen from Figures 4b and 9c. By adopting a more realistic phase diagram of crustal materials where the phase transition occurs over a range of pressure [e.g., *Fumagalli and Klemme,* 2015], a more realistic thickness of the crust would be obtained.

5. Conclusion

The numerical models presented here suggest that the mantle has evolved in the four stages illustrated in Figure 11 in Mars owing to the magmatism-mantle upwelling feedback, and that the plume magmatism of Stage III is responsible for the observed active magmatism and clement surface environment of early Mars.

Appendix A: The basic equations

The momentum equation in its non-dimensional form is

$$-\nabla^* p^* - Ra\ \delta\rho^* \mathbf{e_z} + \nabla^* \cdot [\eta^* (\nabla^* \mathbf{U}^* +^t \nabla^* \mathbf{U}^*)] = \mathbf{0}, \quad \text{(A1)}$$

where the asterisks stand for normalized quantities. The length is normalized by the box depth d, the time by d^2/κ where κ is the thermal diffusivity, and the viscosity by the reference viscosity η_0. $\boldsymbol{U}^*$ is the matrix velocity, p^* the dynamic pressure, and $\boldsymbol{e}_z$ the vertical unit vector pointing upward. The density deviation $\delta\rho^*$ is defined by

$$\begin{aligned}\delta\rho^* \equiv\ & [(1-\phi)\rho_s + \phi\rho_l - \rho_0]\,/\rho_0\alpha\Delta T \\ & = -T^* + \beta_s^*(1-\xi_b) + \phi\,(\beta_l^* - \beta_s^*)(1-\xi_l) - \ \phi\Delta_l^*\,[1+\beta_l\,(1-\xi_l)] \quad \text{(A2)}\end{aligned}$$

where $\beta^*_{s,l} = \beta_{s,l}/\alpha\Delta T$ and $\Delta_l^* = \Delta_l/\alpha\Delta T$, while the Rayleigh number Ra is defined by

$$Ra = \rho_0\ \Delta {\rm T} {\rm g} d^3/\eta_0\kappa. \quad \text{(A3)}$$

(In Equations (A2) and (A3), the temperature is normalized by $\Delta T = \Delta h/C_p$. For the constants in these equations, see Table 1.) The continuity equation is

$$\nabla^* \cdot \mathbf{U}^* = \ -\nabla^* \cdot [\phi\,(\mathbf{u}^* - \mathbf{U}^*)], \quad \text{(A4)}$$

where $\boldsymbol{u}^*$ is the velocity of magma. I neglected the volume change from melting in this equation [*Boukare and Ricard,* 2017]. The relative velocity $\mathbf{u}^* - \mathbf{U}^*$ is proportional to the density difference between magma and matrix:

$$\phi\,(\mathbf{u}^* - \mathbf{U}^*) = P_m \left(\frac{\phi}{\phi_0}\right)^3 (\rho_s^* - \rho_l^*)\,\mathbf{e}_z \quad \text{(A5)}$$

where $_0$ is the reference content of magma, and the reference permeability P_m is

$$P_m = k_\phi^0 \rho_0 \alpha \Delta T g d / \mu \kappa. \quad \text{(A6)}$$

Here, k_ϕ^0 is the permeability at $= _0$, and is the viscosity of magma; the effect of deformation of matrix on magma migration [*McKenzie,* 1984] is neglected. The value of k_ϕ^0 in Table 1 is taken from *McKenzie* [1984] and *Miller et al.* [2014], while that of μ from *Dingwell* [2015]. Equation (A5) implies that magma does not penetrate into subsolidus regions where $\phi = 0$. At shallow depth-levels, however, magma can penetrate into such regions by forming cracks in host rocks. I assumed that this type of magma-migration can occur in the crust and replaced ϕ in Equation (A5) with $\max(\phi,\ \phi_0)$ for $1 - z^* < d^*_{\rm BE}$.

The transport equation for the reduced enthalpy h^* defined by Equation (9) is

$$\frac{\partial h^*}{\partial t^*} + \nabla^* \cdot (h^* \mathbf{U}^*) = -\nabla^* \cdot [\phi h_l^* (\mathbf{u}^* - \mathbf{U}^*)] + \nabla^{*2} T^* + Q^* + \nabla^* \cdot (\kappa^*_{\rm edd} \nabla^* h^*) - N \phi \Delta_l \mathbf{u}^* \cdot \mathbf{e}_z, \quad \text{(A7)}$$

where Q^* is the internal heating rate, and

$$N = g d / \Delta h. \quad \text{(A8)}$$

Here, the reduced enthalpy is normalized by the latent heat of melting h. The first term on the right-hand side of Equation (A7) stands for the contributions from transport by magma-migration, the second to fourth terms for the contribution from entropy change, and the fifth term for the contribution from pressure change. (Here, $\kappa^*_{\rm edd}$ is the eddy diffusivity for a turbulent flow of magma in largely molten regions normalized by κ; matrix disintegrates, and the flow of magma becomes turbulent at higher than a threshold, about 0.4 [*Solomatov*, 2015]. To simulate the effects of this turbulent flow, I assumed that $\kappa^*_{\rm edd}$ gradually increases from 0 at $= 0$ to 100 at $= 0.4$; $\kappa^*_{\rm edd}$ is clipped at 100 for > 0.4.)

The temperature of the heat bath (i.e., the core) changes with time according to

$$M \frac{dT^*_{\rm hb}}{dt^*} = -h^*_{\rm fCMB} \quad \text{(A9)}$$

where $h^*_{\rm fCMB}$ is the heat flow on the CMB calculated from the temperature distribution in the box, and M is the ratio of the heat capacity of the core to that of the mantle.

The mass transport equation is

$$\frac{\partial \xi_b}{\partial t^*} + \nabla^* \cdot (\xi_b \mathbf{U}^*) = -\nabla^* \cdot [\phi \xi_l (\mathbf{u}^* - \mathbf{U}^*)] + \nabla^* \cdot (\kappa^*_{\rm edd} \nabla^* \xi_b). \quad \text{(A10)}$$

The first term on the right-hand side stands for the contribution of mass-transport by migrating magma.

The internal heating rate changes with time, as

$$Q^* = Q_{\rm tr} [\Delta Q^* \exp\left(-\tfrac{t^*}{\tau^*}\right) + Q_0^*]. \quad \text{(A11)}$$

Here, the first term in the parenthesis stands for the HPEs with short half-lives (^{40}K and ^{235}U), while the second term for those with long half-lives (^{238}U and ^{232}Th) [*Turcotte and Schubert*, 2002]. The values of ΔQ and Q_0 listed in Table 1 are based on *Wanke and Dreibus* [1994]. On the other hand, $Q^*_{\rm tr}$ stands for the effects of transport by migrating magma and convecting matrix. $Q^*_{\rm tr}$ is normalized so that $\frac{1}{V}\int_V Q^*_{\rm tr} \mathrm{d}V = 1$ holds (the integration extends over the convecting box) and changes with time as

$$\frac{\partial Q^*_{\rm tr}}{\partial t^*} + \nabla^* \cdot (Q^*_{\rm tr}\mathbf{U}^*) = -\nabla^* \cdot [\phi Q^*_{\rm ltr}(\mathbf{u}^* - \mathbf{U}^*)] + \nabla^* \cdot (\kappa_{\rm edd}\nabla^* Q^*_{\rm tr}) \quad \text{(A12)}$$

where $Q^*_{\rm ltr} = Q^*_{\rm tr}/[\phi + D(1-\phi)]$ is the HPE-content in magma, and D is the partition coefficient.

The basic equation that describes water-transport is

$$\frac{\partial \phi_w}{\partial t^*} + \nabla^* \cdot (\phi_w \mathbf{U}^*) = -\nabla^* \cdot [\phi\phi_{\rm wl}(\mathbf{u}^* - \mathbf{U}^*)] + F^* + \nabla^* \cdot (\kappa^*_{\rm edd}\nabla^*\phi_w). \quad \text{(A13)}$$

Here, $\phi_{\rm wl} \equiv \phi_w/\phi$ is the content of water in magma, and F^* expresses the effect of outgassing: I assumed that water contained in magma is all outgassed, when the magma ascends to the topmost 10 km of the convecting box.

The boundary conditions for Equations (A10), (A12), and (A13) are that there are no convective and diffusive fluxes of ξ_b, ξ_l , $Q^*_{\rm tr}$ and ϕ_w through all the boundaries.

The basic equations are discretized by a finite difference method. The employed mesh is uniform and contains 300 (horizontal) times 150 (vertical) mesh points for calculation of the continuity and momentum equations; twice that resolution is employed for calculation of the transport equations.

Appendix B. The three components of velocity field and the MMU feedback

I calculated the three components of the velocity field $\mathbf{U}$ presented in Figures 4 to 7 as follows: the component driven by thermal and compositional buoyancy $\mathbf{U}^{\rm TC}$ is calculated from Equations (A1), (A2) with $\phi = 0$, and

$$\nabla^* \cdot \mathbf{U}^* = 0; \quad \text{(B1)}$$

the component driven by melt-buoyancy $\mathbf{U}^{\rm melt}$ from Equations (A1) with

$$\delta\rho^* = \phi(\beta^*_l - \beta^*_s)(1-\xi_l) - \phi\Delta^*_l[1 + \beta_l(1-\xi_l)] \quad \text{(B2)}$$

and (B1); the component driven by the volume change of matrix caused by magma-migration $\mathbf{U}^{\rm dv}$ from Equations (A1) with $\delta\rho^* = 0$, (A4) and (A5).

This decomposition of convective velocity field reveals the nature of the MMU feedback (see Figure B1). There are two paths in the MMU feedback. One occurs through $\mathbf{U}^{\rm melt}$ and is denoted as the MMUb feedback in Figure B1; the buoyancy of magma generated by a mantle upwelling flow intensifies the upwelling flow itself. This feedback becomes substantial, when the Rayleigh number defined with the viscosity of convecting part of the mantle exceeds a

threshold. The threshold is around 10^6 to 10^7 and increases with increasing Pm, implying that the MMUb feedback is more important at lower Pm, as shown in Figure 6 of *Ogawa* [2018]. The MMUb feedback has been discussed in earlier studies, too [*Tackley and Stevenson* 1993; *Barnouin-Jha and Parmentier* 1997; *Raddick et al.* 2002; *Hernlund et al.* 2008a,b]. The other occurs through $\mathbf{U}^{\rm dv}$ and is denoted as the MMUc feedback in Figure B1; an upward migration of magma in a partially molten region causes an expansion and contraction of the matrix at the top and base, respectively, of the region, and this volume change enhances the original upwelling flow that causes the partial melting, when the viscosity is spatially variable (see below). The MMUc feedback is more substantial at higher Pm, since $\mathbf{U}^{\rm dv}$ is proportional to Pm (see Equations (A4) and (A5)). The feedback, however, does not depend on Ra, since $\mathbf{U}^{\rm dv}$ is calculated from Equation (A1) with $\delta\rho^* = 0$.

A further decomposition of $\mathbf{U}^{\rm dv}$ into the potential part and solenoidal part more clearly shows the nature of the MMUc feedback:

$$\mathbf{U}^{\rm dv} = -\nabla\psi + \nabla \times \mathbf{A}, \quad \text{(B3)}$$

where ψ is calculated from Equations (A4) and (A5). The potential flow is the counter flow of upward migration of magma and points downward in partially molten regions. The potential flow, therefore, cannot induce the MMUc feedback by itself. When the viscosity is spatially variable, however, the potential part induces the solenoidal part through Equation (A1). The solenoidal flow can point upward in partially molten regions to cause the MMUc feedback, as illustrated in Figure B1b. The feedback becomes more significant, as viscosity variation becomes larger in the mantle surrounding the partially molten region. In Figure 4c, the MMUc feedback is significant, since the partially molten region extends from the asthenosphere to the surface boundary beneath the black bar in the figure, and upwelling magma pushes the stiff lithosphere aside to cause a convective circulation that extends over the entire convecting box. In Figure 5, however, the partially molten head of the upwelling plume is mostly within the asthenosphere. Therefore, the lithosphere remains almost stagnant, and the volume change of matrix due to magma-migration only locally induces a potential flow that points downward beneath the lithosphere (see $\mathbf{U}^{\rm dv}$ in Figure 5c). This is the reason why the MMUc feedback does not operate.

Acknowledgement. The author acknowledges the financial support from KAKENHI20H04606 by MEXT of Japan. Figures 2 to 7 were drawn with the Generic Mapping Tools (GMT) by Paul Wessel and W.H.F. Smith.

Data availability. The original data used to produce Figures 2-7 and Table 3 are available at https://doi.org/10.6084/m9.figshare.14616150.

References

Acuna, M.H. et al (1999), Global distribution of crustal magnetization discovered by the Mars Global Surveyor MAG/ER experiment, *Science, 284,* 790-793.

Ballmer, M.D., D.L. Lourenco, K. Hirose, R. Caracas, and R. Nomura (2017),

Reconciling magma-ocean crystallization models with the present-day structure of the Earth's mantle, *Geochem. Geophys. Geosyst.*, *18,* 2785-2806, doi:10.1002/2017GC006917.

Barnouin-Jha, K., and E.M. Parmentier (1997), Buoyant mantle upwelling and crustal production at oceanic spreading centers: On-axis segmentation and off-axis melting, *J. Geophys. Res., 102,* 11979-11989.

Boukare, C.-E. and Y. Ricard (2017), Modeling phase separation and phase change for magma ocean solidification dynamics, *Geochem. Geophys. Geosyst.*, *18,* 3385-3404, doi:10.1002/2017GC006902.

Boukare, C.-E., E.M. Parmentier, and S.W. Parman (2018), Timing of mantle overturn during magma ocean solidification, *Earth Planet. Sci. Lett., 491,*216-225. https://doi.org/10.1016/j.epsl.2018.03.037

Bouley, S., D. Baratoux, I. Matsuyama, F. Forget, A. Sejourne, M. Turbet, and F. Costard (2016), Late Tharsis formation and implications for early Mars, *Nature, 531,* 344-347.

Breuer, D., and T. Spohn (2003), Early plate tectonics versus single-plate tectonics on Mars: Evidence from magnetic field history and crust evolution, *J. Geophys. Res.: Planets, 108*, 5072, doi:10.1029/2002JE001999.

Broquet, A., and M.A. Wieczorek (2019), The gravitational signature of Martian volcanoes, *J. Geophys. Res.: Planets, 124,* 2054–2086. https://doi.org/10.1029/2019JE005959

Carr, M. H., and J. W. Head (2003), Ocean on Mars: an assessment of the observational evidence and possible fate, *J. Geophys. Res., 108* (E5), 5042. doi:10.1029/2002JE001963.

Carr, M.H. and J.W. Head (2010), Geologic history of Mars, *Earth Planet. Sci. Lett., 294,* 185-203.

Citron, R.I., M. Manga, and D.J. Hemingway (2018), Timing of oceans on Mars from shoreline deformation, *Nature, 555,* 643-646.

Debaille, V., A.D. Brandon, C. O'Neill, Q.-Z. Yin, and B. Jacobsen (2009), Early Martian mantle overturn inferred from isotopic composition of nakhlite meteorites, *Nature Geosci., 2,* 548-552, doi:10.1038/NGEO579.

Di Achille, G., and B.M. Hynek (2010), Ancient ocean on Mars supported by global distribution of deltas and valleys, *Nature Geosci., 3,* 459-463.

Ding, M., J. Lin, C. Gu, Q. Huang, and M.T. Zuber (2019), Variations in Martian lithospheric strength based on gravity/topography analysis. *J. Geophys. Res.: Planets*, *124*, 3095-3118, https://doi.org/10.1029/2019JE005937.

Dingwell, D.B. (2015), Properties of rocks and minerals, diffusion, viscosity, and flow of melts, *in "Mineral physics"* (ed. Price, G.D., Stixrude, L.), *Treatise on*

Geophysics, vol. 2, 473-486, Elsevier, Amsterdam, Netherland. https://doi.org/10.1016/B978-0-444-53802-4.00043-9

Dumoulin, C., M.-P. Doin, and L. Fleitout (1999), Heat transport in stagnant lid convection with temperature- and pressure-dependent Newtonian or non-Newtonian rheology, *J. Geophys. Res.: Solid Earth,104,* 12750-12777. **https://doi.org/10.1029/1999JB900110**

Ehlmann, B.L., J.F. Mustard, S.L. Murchie, J.-P. Bibring, A. Meunier, A.A. Fraeman, and Y. Langevin (2011), Subsurface water and clay mineral formation during the early history of Mars, *Nature, 479,* 53-60.

Ehlmann, B. L., et al. (2016), The sustainability of habitability on terrestrial planets: Insights, questions, and needed measurements from Mars for understanding the evolution of Earth-like worlds, *J. Geophys. Res.: Planets, 121,* 1927-1961. doi:10.1002/2016JE005134

Elkins-Tanton, L.T., S.E. Zaranek, E.M. Parmentier, and P.C. Hess (2005), Early magnetic field and magmatic activity on Mars from magma ocean cumulate overturn, *Earth Planet. Sci. Lett., 236,* 1-12.

Fassett, C.I. and J.W. Head (2011), Sequence and timing of conditions on early Mars, *Icarus, 211,* 1204-1214.

Foley, C.N., M. Wadhwa, L.E. Borg, P.E. Janney, R. Hines, and T.L. Grove (2005), The early differentiation history of Mars from ^{182}W-^{142}Nd isotope systematics in the SNC meteorites, *Geochim. Cosmochim. Acta, 69* (18), 4557-4571.

Fraeman, A.A., J. Korenaga (2010), The influence of mantle melting on the evolution of Mars, *Icarus, 210(1)*, 43-57. doi:10.1016/j.icarus.2010.06.030.

Fumagalli, P., and S. Klemme (2015), Mineralogy of the Earth: phase transitions and mineralogy of the upper mantle, *in "Mineral physics"* (ed. Price, G.D., Stixrude, L.), *Treatise on Geophysics, vol. 2*, 7-31, Elsevier, Amsterdam, Netherland. http://dx.doi.org/10.1016/B978-0-444-53802-4.00052-X

Gilfoy, F., and J. Li (2020), Thermal state and solidification regime of the Martian core: Insights from the melting behavior of FeNi-S at 20 GPa, *Earth Planet. Sci. Lett., 541,* 116285. https://doi.org/10.1016/j.epsl.2020.116285

Greeley, R., and B.D. Schneid (1991), Magma generation on Mars: Amounts, rates, and comparisons with Earth, Moon, and Venus, *Science, 254,* 996-998.

Grott, M, A. Morschhauser, D. Breuer, and E. Hauber (2011), Volcanic outgassing of CO_2 and H_2O on Mars, *Earth Planet. Sci. Lett., 308,* 391-400.

Grott, M., et al. (2013), Long-term evolution of the Martian crust-mantle system, *Space Sci. Rev., 174,* 49-111. https://doi.org/10.1007/s11214-012-9948-3

Halevy, I., and J.W. Head (2014), Episodic warming of early Mars by punctuated volcanism, *Nature Geosci., 7,* 865-868. Doi:10.1038/NGEO2293.

Hauck, S.A., and R.J. Phillips (2002), Thermal and crustal evolution of Mars, *J. Geophys. Res.: Planets, 107*, 6-1-6-19, doi:10.1029/2001JE001801.

Head, J.W., M.A. Kreslavsky, and S. Pratt (2002), Northern lowlands of Mars: Evidence for widespread volcanic flooding and tectonic deformation in the Hesperian Period, *J. Geophys. Res., 107* (E1), 3-1-3-29, doi: 10.1029/2000JE001445

Hernlund, J.W., P.J. Tackley, and D.J. Stevenson (2008a) Buoyant melting instabilities beneath extending lithosphere: 1. Numerical models, *J. Geophys. Res.: Solid Earth, 113,* B04405, doi:10.1029/2006JB004862.

Hernlund, J. W., D.J. Stevenson, and P.J., Tackley (2008b) Buoyant melting instabilities beneath extending lithosphere: 2. Linear analysis, *J. Geophys. Res.: Solid Earth, 113,* B04406, doi:10.1029/2006JB004863.

Hoke, M.R.T., B.M. Hynek, and G.E. Tucker (2011), Formation timescales of large Martian valley networks, *Earth Planet. Sci. Lett., 312,*1-12. doi:10.1016/j.epsl2011.09.053

Irifune, T., and A.E. Ringwood (1993), Phase transitions in subducted oceanic crust and buoyancy relationships at depths of 600-800 km in the mantle, *Earth Planet. Sci. Lett., 117*, 101-110. https://doi.org/10.1016/0012-821X(93)90120-X

Keller, T., and P.J. Tackley (2009), Towards self-consistent modeling of the martian dichotomy: The influence of one-ridge convection on crustal thickness distribution, *Icarus, 202,* 429-443. https://doi.org/10.1016/j.icarus.2009.03.029

Kiefer, W.S. and Q. Li (2009), Mantle convection controls the observed lateral variation in lithospheric thickness on present-day Mars, *Geophys. Res. Lett., 36,* L18203, doi:/10.1029/2009GL039827.

Kruijer, T.S., L.E. Borg, J. Wimpenny, and C.K. Sio (2020), Onset of magma ocean solidification on Mars inferred from Mn-Cr chronometry, *Earth Planet. Sci. Lett., 542*, 116315. https://doi.org/10.1016/j.epsl.2020.116315

Kruijer, T.S., T. Kleine, L.E. Borg, G.A. Brennecka, A.J. Irving, A. Bischoff, and C.B. Agee (2017), The early differentiation of Mars inferred from Hf-W chronometry, *Earth Planet. Sci. Lett., 474*, 345-354. https://doi.org/10.1016/j.epsl.2017.06.047

Lillis, R.J., S. Robbins, M. Manga, J.S. Halekas, and H.V. Frey (2013), Time history of the Martian dynamo from crater magnetic field analysis, *J. Geophys. Res.: Planets, 118,* 1488-1511, doi:10.1002/jgre20105.

Litasov, K.D., A. Shatskiy, and E. Ohtani (2014), Melting and subsolidus phase relations in peridotite and eclogite system with reduced C-O-H fluid at 3-16 GPa, *Earth Planet. Sci. Lett., 391,* 87-99. https://doi.org/10.1016/j.epsl.2014.01.033

Maurice, M., N. Tosi, H. Samuel, A.-C. Plesa, C. Hüttig, and D. Breuer (2017), Onset of solid-state mantle convection and mixing during magma ocean solidification, *J. Geophys. Res. Planets*, 122, 577-598. doi:10.1002/2016JE005250.

McCubbin, F.M., E.H. Hauri, S.M. Elardo, K.E. Vander Kaaden, J. Wang, and C.K. Shearer Jr. (2012), Hydrous melting of the martian mantle produced both depleted and enriched shergottites, *Geology, 40* (8)*,* 683-686,

McKenzie, D. (1984) The generation and compaction of partially molten rock, *J. Petrol., 25,* 713-765. https://doi.org/10.1093/petrology/25.3.713

Miller, K.J., W.-I. Zhu, L.G.J. Montesi, and G.A. Gaetani (2014) Experimental quantification of permeability of partially molten mantle rock, *Earth Planet. Sci. Lett., 388,* 273-282. https://doi.org/10.1016/j.epsl.2013.12.003

Morschhauser, A., M. Grott, and D. Breuer (2011), Crustal recycling, mantle dehydration, and the thermal evolution of Mars, *Icarus, 212,* 541-558. https://doi.org/10.1016/j.icarus.2010.12.028

Mouginot, J., A. Pommerol, P. Beck, W. Kofman, and S.M. Clifford (2012), Dielectric map of the Martian northern hemisphere and the nature of plain filling materials, *Geophys. Res. Lett., 39,* L02202, doi:10.1029/2011GL050286.

Nimmo, F., and D.J. Stevenson (2000) Influence of early plate tectonics on the thermal evolution and magnetic field of Mars, *J. Geophys. Res.: Planets, 105* (E5), 11969-11979. **https://doi.org/10.1029/1999JE001216**

Norman, M.D. (1999), The composition and thickness of the crust of Mars estimated from rare earth elements and neodymium-isotopic composition of Martian meteorites, *Metor. Plaent. Sci., 34,* 439-449.

Ogawa, M. (2018), Magmatic differentiation and convective stirring of the mantle in early planets: the effects of the magmatism-mantle upwelling feedback, *Geophys. J. Int., 215,* 2144-2155. https://doi.org/10.1093/gji/ggy413

Ogawa, M. (2020), Magmatic differentiation and convective stirring of the mantle in early planets-2: the effects of properties of mantle materials, *Geophys. J. Int., 220,* 1409-1420. https://doi.org/10.1093/gji/ggz499

Ogawa, M. and T. Yanagisawa (2012), Two-dimensional numerical studies on the effects of water on Martian mantle evolution induced by magmatism and solid-state mantle convection, *J. Geophys. Res., 117,* E06004, doi:10.1029/2012JE004054.

Olsen, A.A., and J.D. Rimstidt (2007), Using a mineral lifetime diagram to evaluate the persistence of olivine on Mars, *Amer. Mineral., 92,* 598-602. doi:10.2138/am.2007.2462

Phillips, R.J., et al. (2001), Ancient geodynamics and global-scale hydrology on Mars, *Science, 291,* 2587-2591. DOI: 10.1126/science.1058701

Plesa, A.-C., N. Tosi, and D. Breuer (2014), Can a fractionally crystallized magma ocean explain the thermo-chemical evolution of Mars?, *Earth Planet. Sci. Lett., 403,* 225-235. https://doi.org/10.1016/j.epsl.2014.06.034

Plesa, A.-C., N. Tosi, M. Grott, and D. Breuer (2015), Thermal evolution and Urey ratio of Mars, *J. Geophys. Res. Planets, 120,* 995–1010, doi:10.1002/2014JE004748.

Plesa, A.-C., M. Grott, N. Tosi, D. Breuer, T. Spohn, and M. A. Wieczorek (2016), How large are present-day heat flux variations across the surface of Mars?, *J. Geophys. Res. Planets*, *121*, 2386-2403, doi:10.1002/2016JE005126.

Plesa, A.-C., S. Padovan, N. Tosi, D. Breuer, M. Grott, M.A. Wieczorek, et al. (2018), The thermal state and interior structure of Mars. *Geophys. Res. Lett.*, *45*, 12,198–12,209. https://doi.org/10.1029/2018GL080728

Raddick, M. J., E.M. Parmentier, and D.S. Scheirer (2002) Buoyant decompression melting: A possible mechanism for intraplate volcanism, *J. Geophys. Res.: Solid Earth*, *107*(B10), ECV 7-1-ECV-7-14, doi:10.1029/2001JB000617.

Ramirez, R.M., Kopparapu, R., Zugger, M.E., Robinson, T.D., Freedman, R., and Kasting, J.F. (2014), Warming early Mars with CO_2 and H_2, *Nature Geosci., 7,* 59-63. doi:10.1038/NGEO2000.

Ruedas, T., P.J. Tackley, S.C. Solomon (2013a), Thermal and compositional evolution of the Martian mantle: effects of phase transitions and melting, *Phys. Earth Planet. Inter., 216,* 32-58 https://doi.org/10.1016/j.pepi.2012.12.002

Ruedas, T., P.J. Tackley, S. Solomon (2013b), Thermal and compositional evolution of the Martian mantle: effects of water, *Phys. Earth Planet. Inter., 220,* 50-72. https://doi.org/10.1016/j.pepi.2013.04.006

Ruiz, J., P.J. McGovern, A. Jimenez-Diaz, V. Lopez, J.-P. Williams, B.C. Hahn, and R. Tejero (2011), The thermal evolution of Mars as constrained by paleoheat flows, *Icarus, 215,* 508-517. https://doi.org/10.1016/j.icarus.2011.07.029

Samuel, H., M.D Ballmer, S. Padovan, N. Tosi, A. Rivoldini, and A.-C. Plesa (2021), The thermo-chemical evolution of Mars with a strongly stratified mantle, *J. Geophys. Res. Planets, 126,* doi:10.1029/2020JE006613.

Sandu, C. and W.S. Kiefer (2012), Degassing history of Mars and the lifespan of its magnetic dynamo, *Geophys. Res. Lett., 39,* L03201, doi:10.1029/2011GL050225.

Sanloup, C., J.W.E. Drewitt, Z. Konopkova, P. Dalladay-Simpson, D.M. Morton, N. Rai, W. van Westrenen, and W. Morgenroth (2013), Structural change in molten basalt at deep mantle condition, *Nature, 503,* 104-107. https://doi.org/10.1038/nature12668

Scheinberg, A., L. T. Elkins-Tanton, and S. J. Zhong (2014), Timescale and morphology of Martian mantle overturn immediately following magma ocean solidification, *J. Geophys. Res. Planets, 119,* 454–467, doi:10.1002/2013JE004496

Scheller, E.L., B.L. Ehlmann, R. Hu, D.J. Adams, and Y.L. Yung (2021), Long-term drying of Mars by sequestration of ocean-scale volumes of water in the crust, *Science, 372,* 56-62.

Schumacher, S., and D. Breuer (2007), An alternative mechanism for recent volcanism on Mars, *Geophys. Res. Lett., 34,* L14202. Doi:10.1029/2007GL030083.

Sekhar, P. and S.D. King (2014), 3D spherical models of Martian mantle convection constrained by melting history, *Earth Planet. Sci. Lett., 388,* 27-37. https://doi.org/10.1016/j.epsl.2013.11.047

Silber, R.E., R.A. Secco, W. Yong, and J.A.H. Littleton (2019). Heat flow in Earth's core from invariant electrical resistivity of Fe-Si on the melting boundary to 9 GPa: Do light elements matter?, *J. Geophys. Res.: Solid Earth, 124,* 5521-5543. https://doi.org/10.1029/2019JB017375

Solomatov, V. (2015). Magma oceans and primordial mantle differentiation, *in "Evolution of the Earth"* (ed. Stevenson, D.J.), *Treatise on Geophysics, vol. 9,* pp. 82-103, Elsevier, Amsterdam, Netherland.

Sramek, O., and S. Zhong (2012), Martian crustal dichotomy and Tharsis formation by partial melting coupled to early plume migration, *J. Geophys. Res., 117,* E01005, doi:10.1029/2011JE003867.

Tackley, P.J. and D.J. Stevenson, (1993), A mechanism for spontaneous perpetuating volcanism o the terrestrial planets, in "*Flow and Creep in the solar system: Observations, modeling, and theory,* (ed. Stone, D.B., Runcorn, S.K.), 307-321, Kluwer Academic Publishers, Nederland.

Tosi, N., A.-C. Plesa, and D. Breuer (2013), Overturn and evolution of a crystallized magma ocean: A numerical parameter study for Mars, *J. Geophys. Res. Planets, 118*, 1512–1528, doi:10.1002/jgre.20109.

Turcotte, D.L., and G. Schubert (2002) "*Geodynamics*", 2'nd ed., Cambridge Univ. Press., U.K., 456 pp.

Vervelidou, F., V. Lesur, M. Grott, A. Morschhauser, R.J. Lillis (2017), Constraining the date of the Martian dynamo shutdown by means of crater magnetization signatures, *J. Geophys. Res., 122,* 2294-2311, https://doi.org/10.1002/2017JE005410

Wanke, H., and G. Dreibus (1994), Chemistry and accretion of Mars, *Phil. Trans. R. Soc. London, Ser. A, 349*, 2134–2137. https://doi.org/10.1098/rsta.1994.0132

Werner, S.C. (2009), The global Martian volcanic evolutionary history, *Icarus, 201,* 44-68. https://doi.org/10.1016/j.icarus.2008.12.019

Wernicke, L. J., & Jakosky, B. M. (2021), Martian hydrated minerals: A significant water sink. *J. Geophys. Res.: Planets*, *126*, e2019JE006351. https://doi.org/10.1029/2019JE006351

Wordsworth, R., A.H. Knoll, J. Hurowitz, M. Baum, B.L. Ehlmann, J.W. Head, and K. Steakley (2021), A coupled model of episodic warming, oxidation and geochemical transitions on early Mars, *Nature Geosci., 14,* 127-132. doi.org/10.1038/s41561-021-00701-8.

Yoshizaki, T. and W.F. McDonough (2020), The composition of Mars, *Geochim. Cosmochim. Acta, 273,* 137-162. https://doi.org/10.1016/j.gca.2020.01.011

Zaranek, S. E., and E. M. Parmentier (2004), Convective cooling of an initially stably stratified fluid with temperature-dependent viscosity: Implications for the role of solid-state convection in planetary evolution, *J. Geophys. Res., 109,* B03409, doi:10.1029/2003JB002462.

Zuber, M.T., et al. (2000), Internal structure and early thermal evolution of Mars from Mars Global Surveyor topography and gravity, *Science, 287,* 1788-1793.

Table 1. The constants and their values.

Symbol	Meaning	value
d	Depth of the convecting box	1000 km
d_{BE}	Depth of the basalt-eclogite transition	km
ρ_0	Reference density	kg m^{-3}
	Thermal expansivity	3×10^{-5} K^{-1}
$\beta_s,\ \beta_l$	Sensitivity of density to composition; see Eqs. (1) to (3).	For β_s, see Eq. (2); $\beta_l = 0.067$
Δ_l^0	The constants in	500 km
λ_∞	Equation (4)	
T_{ref}	Reference temperature	K
T_s^0	Dry solidus temperature on the surface	K
ϕ_{w0}	Reference water-content	ppm
T	Temperature scale	h/C_p
h	Latent heat of melting at $z = d$	kJ kg^{-1}
C_p	Specific heat	J K^{-1}kg^{-1}
	Thermal diffusivity	$6 \times 10^{-7} m^2 s^{-1}$
g	Gravitational acceleration	m s^{-2}
k_ϕ^0	Permeability at $\phi = \phi_0$	$^{-14}$ -10^{-13} m^2
μ	melt-viscosity	-10 Pa s
$_0$	Reference melt-content	

Symbol	Meaning	value
ΔQ	The parameters for	pW kg^{-1}
Q_0	internal heating rate;	4.0 pW kg^{-1}
τ	see Eq. (A11)	1.5 Gyr
D	Partition coefficient of HPEs (solid/melt)	
N	See Eq. (A8)	

Table 2. The default values of model parameters.

symbol	meaning	default value
E	Sensitivity of viscosity to temperature; see Eq. (5)	5.7/ΔT K^{-1}
V_p	Sensitivity of viscosity to depth	2.3
V_W	Sensitivity of viscosity to water-content	2.3
ΔT_s	Solidus reduction by water; see Eq. (8).	250 K
$T_{\rm is}$	The initial temperature at the top; see Figure 1b	2200 K
$T_{\rm ic}$	The initial temperature of the core.	$T_{\rm is}$
M	The ratio of heat capacity of the core to that of the mantle	0.18
P_m	The reference permeability defined by Eq. (A6)	3.2

Table 3. The values of the free parameters Ra, $\mathbf{T_{ib}}$, and $\overset{\rm init}{\mathbf{w}}$ and a summary of the results.

Case #	Ra	$T_{\rm ib}$	$\phi_w^{\rm init}$	comment	$t^{10}_{\rm CMB}$	$t^{0}_{\rm CMB}$	$t^{b}_{\rm MAG}$	$t^{e}_{\rm MAG}$	$q^{b}_{\rm crst}$	$q^{e}_{\rm crst}$	$d^{b}_{\rm crst}$
			ppm		Myr	Myr	Gyr	Gyr			km
H10-000	3.20E+06	1000	0		413	566	0.8	2.02	0.211	0.553	88
H10-025	3.20E+06	1000	250		317	518	0.54	1.85	0.227	0.517	80
H10-025a	3.20E+06	1000	250	Vw=6.9	238	466	0.59	2.19	0.25	0.476	74
H10-025b	3.20E+06	1000	250	M=0.64	439		0.56	1.66	0.243	0.587	78
H10-025c	3.20E+06	1000	250	Pm=0.32	354	513	0.49	2.48	0.19	0.386	61
H10-050	3.20E+06	1000	500		233	519	0.65	2.2	0.262	0.446	68
H10-050a	3.20E+06	1000	500	Vw = 0	280	566	0.63	1.97	0.247	0.474	68
H10-050b	3.20E+06	1000	500	Vw = 4.6	212	460	0.68	3.06	0.249	0.432	68
H10-050c	3.20E+06	1000	500	Tic=1800	111	386	1.03	2.78	0.259	0.398	70
H10-050d	3.20E+06	1000	500	Tic=2000	217	455	0.65	2.43	0.252	0.419	65
H10-050e	3.20E+06	1000	500	Pm=0.32	312	460	0.34	2.24	0.189	0.377	67
H10-050f[*3]	3.20E+06	1000	500	Pm=32	143	603			0.39		38
H10-100	3.20E+06	1000	1000		159	481	0.79	2.67	0.279	0.417	62
H12-050	3.20E+06	1200	500		148	466	0.67	1.83	0.286	0.5	69
H12-050a	3.20E+06	1200	500	Pm=0.32	222	344	0.4	2.3	0.207	0.405	67
H12-100	3.20E+06	1200	1000		79	428	0.74	2.24	0.319	0.433	59
H14-025	3.20E+06	1400	250	E=10/ T	79	365	0.8	2.48	0.278	0.606	68

Case #	Ra	$T_{\rm ib}$	$\phi_w^{\rm init}$	comment	$t^{10}_{\rm CMB}$	$t^{0}_{\rm CMB}$	$t^{b}_{\rm MAG}$	$t^{e}_{\rm MAG}$	$q^{b}_{\rm crst}$	$q^{e}_{\rm crst}$	$d^{b}_{\rm crst}$
H14-050	3.20E+06	1400	500		79	423	0.72	2.06	0.312	0.522	67
H14-050a	3.20E+06	1400	500	Vp=6.9/d	175	365	0.44	2.21	0.293	0.481	62
H14-050b	3.20E+06	1400	500	E=10/ T	69	344	0.68	3.54	0.287	0.563	66
H14-050c[*3]	3.20E+06	1400	500	Pm=32	132	508			0.541		38
H14-050d[*4]	3.20E+06	1400	500	Pm=0.32	153	302	0.32	1.83	0.232	0.436	66
H14-100	3.20E+06	1400	1000		74	397	0.43	2	0.366	0.528	66
H16-000	3.20E+06	1600	0		69	280	0.72	1.88	0.276	0.537	72
H16-025	3.20E+06	1600	250		69	296	0.64	2.52	0.329	0.508	68
H16-025a[*5]	3.20E+06	1600	250	Pm=0.32	148	280				0.559	
H16-050	3.20E+06	1600	500		58	270	0.19	2.75	0.352	0.478	64
H16-050a	3.20E+06	1600	500	Ts = 200	63	317	0.22	2.13	0.345	0.519	63
H16-050b	3.20E+06	1600	500	Ts= 300	69	196	0.17	2.67	0.325	0.442	61
H16-050c[*4]	3.20E+06	1600	500	Tis = 1800	21	175	0.13	1.64	0.153	0.555	54
H16-050d	3.20E+06	1600	500	Tis = 2000	58	249	0.19	1.91	0.294	0.579	72
H16-050e	3.20E+06	1600	500	Tis = 2400	79	217	0.28	2.05	0.388	0.555	64
H16-050f	3.20E+06	1600	500	S.I.P.	63	227	0.21	2.53	0.333	0.448	58
H16-050g	3.20E+06	1600	500	M=0.64	79	333	0.23	2.35	0.339	0.507	62
H16-050h	3.20E+06	1600	500	E=10/ T	47	296	0.17	2.27	0.337	0.621	66
H16-050i[*3]	3.20E+06	1600	500	Pm=32	106	339			0.71		49
H16-050j[*5]	3.20E+06	1600	500	Pm=0.32	275	386				0.45	
H16-100	3.20E+06	1600	1000		74	153	0.26	2.14	0.388	0.475	57
H18-000	3.20E+06	1800	0		53	233	0.51	1.65	0.381	0.591	76
H18-000a	3.20E+06	1800	0	Vp = 0	37	190	0.36	2.14	0.359	0.594	74
H18-050	3.20E+06	1800	500		74	132	0.34	2.63	0.409	0.488	61
H18-050a	3.20E+06	1800	500	Vp = 0	48	143	0.16	2.05	0.426	0.545	64
H18-050b	3.20E+06	1800	500	Vw = 0	69	169	0.3	2.61	0.397	0.453	61
H18-050c	3.20E+06	1800	500	S.I.P.	58	164	0.18	2.51	0.373	0.439	69
H18-050d[*4]	3.20E+06	1800	500	Tis=1800	0	0	0.07	1.49	0.193	0.599	72
H18-100	3.20E+06	1800	1000		74	122	1.06	2.63	0.436	0.449	57
M10-025	1.02E+06	1000	250		349	598	0.49	2.98	0.234	0.452	79
M10-025a	1.02E+06	1000	250	Vw=6.9	274	540	0.75	3.25	0.244	0.396	74
M10-050	1.02E+06	1000	500		265	577	0.96	3.02	0.266	0.416	70
M12-050	1.02E+06	1200	500		153	503	0.88	2.78	0.283	0.392	67
M14-050	1.02E+06	1400	500		90	365	0.77	2.45	0.312	0.455	70
M16-050	1.02E+06	1600	500		101	206	0.8	2.48	0.367	0.456	68
M16-050a	1.02E+06	1600	500	S.I.P.	90	212	0.57	1.86	0.329	0.482	65
M18-050	1.02E+06	1800	500		95	164	0.3	2.95	0.36	0.463	67
M18-100	1.02E+06	1800	1000		95	169	0.63	2.86	0.366	0.403	60
L10-050	3.20E+05	1000	500		296	624	1.11	1.74	0.263	0.307	68
L10-050a	3.20E+05	1000	500	Vw=4.6	302	587	0.98	2.75	0.272	0.374	68
L10-050b	3.20E+05	1000	500	Vw=6.9	238	587	0.91	3.26	0.278	0.368	66
L10-100	3.20E+05	1000	1000		206	497	0.98	1.52	0.277	0.287	50
L12-050	3.20E+05	1200	500		190	450	1.19	1.74	0.305	0.314	72
L14-050	3.20E+05	1400	500		116	370	0.93	2.29	0.344	0.404	69

Case #	Ra	$T_{\rm ib}$	$\phi_w^{\rm init}$	comment	$t^{10}_{\rm CMB}$	$t^{0}_{\rm CMB}$	$t^{b}_{\rm MAG}$	$t^{e}_{\rm MAG}$	$q^{b}_{\rm crst}$	$q^{e}_{\rm crst}$	$d^{b}_{\rm crst}$
L16-050	3.20E+05	1600	500		111	302	0.91	1.96	0.391	0.437	73
L16-050a[*3]	3.20E+05	1600	500	Pm=32	88	230			0.5		50
L16-050b[*4]	3.20E+05	1600	500	Pm=0.32	238	392	0.47	1.83	0.461	0.551	73
L16-050c[*5]	3.20E+05	1600	500	Pm=0.032	328	2021				0	
L18-050	3.20E+05	1800	500		122	233	0.6	2.4	0.391	0.425	72

The variable parameters not specified here take their default values listed in Table 2. $t^{10}_{\rm CMB}$ and $t^{0}_{\rm CMB}$ stand for the time when the heat flow on the CMB decreases below 10 $mW\ m^{-2}$ and 0 $mW\ m^{-2}$, respectively, in Stage I; $t^{b}_{\rm MAG}$ and $t^{e}_{\rm MAG}$ the time when the plume magmatism of Stage III begins and ends, respectively; $q^{b}_{\rm crst}$ and $q^{e}_{\rm crst}$ the crustal fraction of HPEs at $t^{b}_{\rm MAG}$ and $t^{e}_{\rm MAG}$, respectively; $d^{b}_{\rm crst}$ and $d^{e}_{\rm crst}$ the average thickness of the crust at $t^{b}_{\rm MAG}$ and $t^{e}_{\rm MAG}$, respectively; $\Delta d = d^{e}_{\rm crst} - d^{b}_{\rm crst}$; $t^{b}_{\rm GAS}$ and $t^{e}_{\rm GAS}$ the time when outgassing starts and ends, respectively, in Stage III; ϕ^{m}_{w} and ϕ^{b}_{w} the water-content in the mantle and the entire box, respectively, at 4.5 Gyr; Δl the total amount of water outgassed in Stage III by plume magmatism, measured by the thickness of Global Equivalent Layer; $\overline{w}$ the average outgassing rate defined by Equation (12); r_m the ratio of peak outgassing rate to $\overline{w}$. Comments: [*1] the data were not collected; [*2]the data were not sampled frequent enough to estimate this quantity; [*3] Stage III does not arise; [*4] Stage II arises only marginally; [*5] Stage II does not arise.

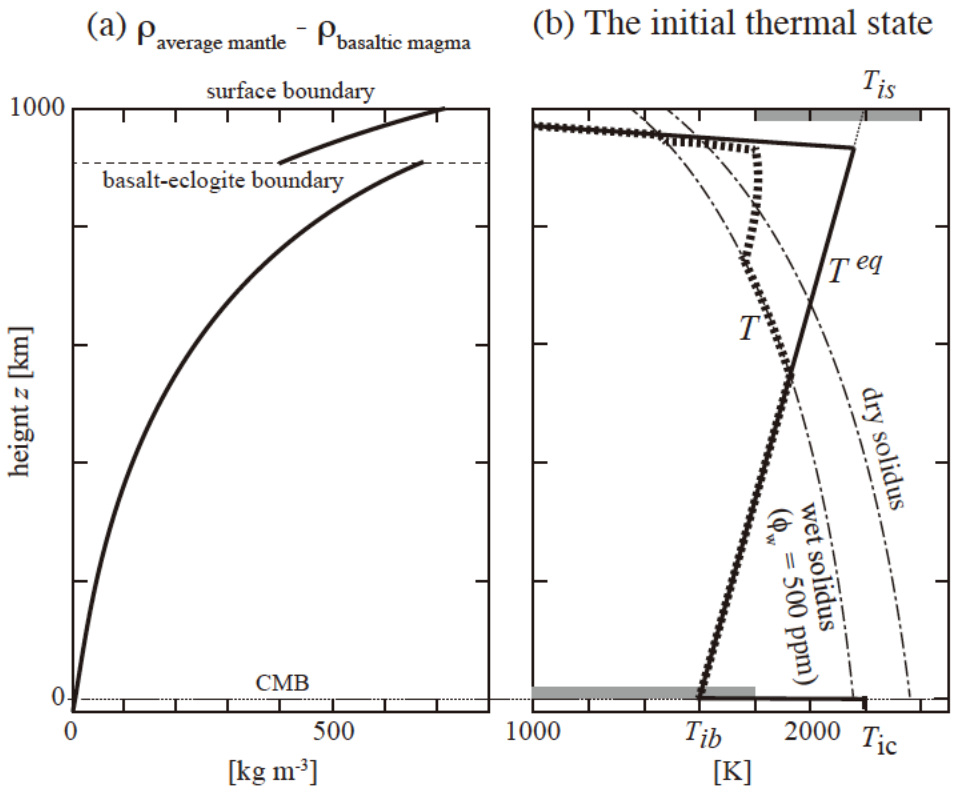

Figure 1. (a) The density difference between magma with $\xi_l = 0.1$ and the average solid mantle material with $\xi_s = 0.64$ plotted against height. (b) An example of the initial distribution of equivalent temperature $T^{\rm eq}$ defined by Equation (11) together with the adopted dry solidus and the wet solidus at $\phi_w = 500\ ppm$, all plotted against height. $T_{\rm is} = 2200\ K$ and $T_{\rm ib} = 1600\ K$ are assumed in this example. Also shown is the initial distribution of temperature calculated from $T^{\rm eq}$ (the thick dotted line). The gray bars indicate the searched ranges of $T_{\rm is}$ and $T_{\rm ib}$.

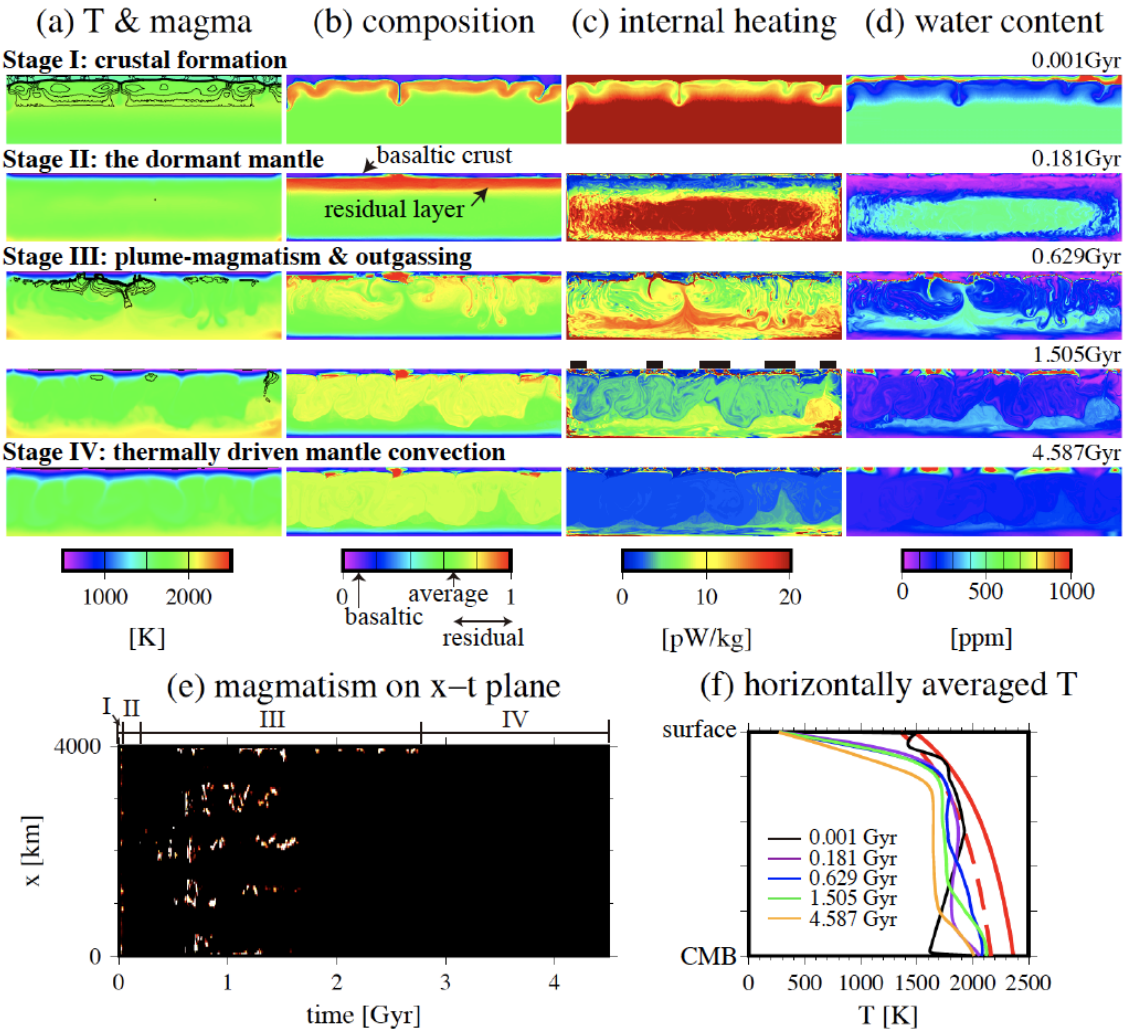

Figure 2. Snapshots of the distributions of (a) temperature T (color) and magma ϕ (contour lines), (b) composition ξ_b, (c) internal heating rate Q, and (d) water-content ϕ_w calculated in Case H16-050 where $Ra = 3.2 \times 10^6$, $\phi_w^{\rm init} = 500\ ppm$, $Pm = 3.2$, and $T_{\rm ib} = 1600\ K$. The contour interval for magma-distribution in (a) is 0.05. In (b), blue color stands for basaltic materials, while yellow to red color for residual materials. Also shown are (e) the location of magma-eruption plotted on the plane of time versus horizontal coordinate x, and (f) the horizontal averages of the temperature-distributions shown in (a) plotted against depth. The Roman numerals in (e) stand for the stages of mantle evolution. The red solid and dashed curves in (f) show the solidus temperature at $\phi_w = 0$ and 500 ppm, respectively.

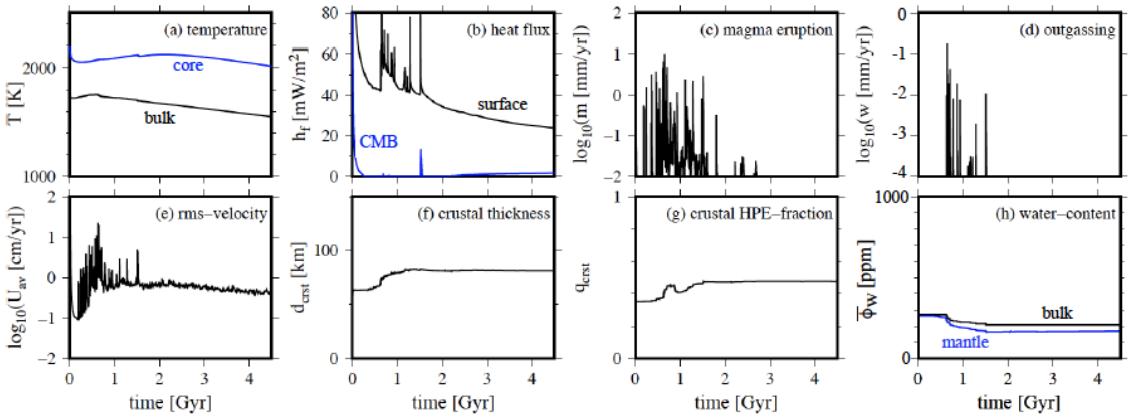

Figure 3. Plotted against time for Case H16-050 are (a) the average temperature in the box (bulk) and the temperature of the core; (b) the horizontal average of heat flux h_f on the surface boundary and the CMB; (c) that of eruption rate of magma m; (d) that of outgassing rate w; (e) the root-mean-square average of matrix-velocity in the box $U_{\rm av}$; (f) the average thickness of the crust $d_{\rm crst}$; (g) the crustal fraction of heat-producing elements (HPEs), i.e. the amount of HPEs contained in the crust normalized by that in the entire box $\underline{q}_{\rm crst}$; (h) the average water-content in the mantle and in the entire box (bulk) $\overline{\phi}_w$.

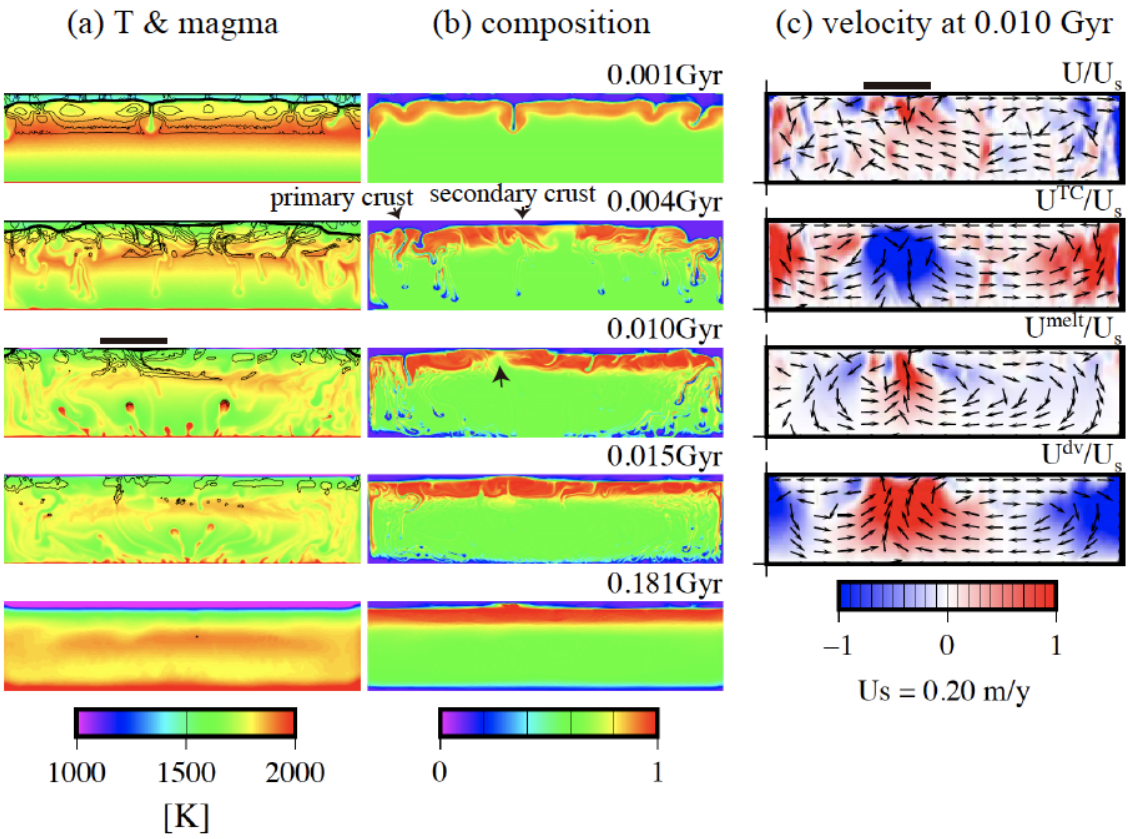

Figure 4. (a) and (b) The same as Figures 2a and 2b, respectively, but for Stages I and II of Case H16-050. (c) Decomposition of the matrix-velocity field $\mathbf{U}$ calculated at 0.010 Gyr into the component driven by thermal and compositional buoyancy $\mathbf{U}^{\mathrm{TC}}$, that driven by melt-buoyancy $\mathbf{U}^{\mathrm{melt}}$, and that driven by the volume-change of matrix that upward migration of magma causes $\mathbf{U}^{\mathrm{dv}}$. The red and blue colors show the regions where the convective flow points upward and downward, respectively. The color scale is normalized by U_s shown at the base of the figure. The arrows express the direction of convective flow but not its magnitude.

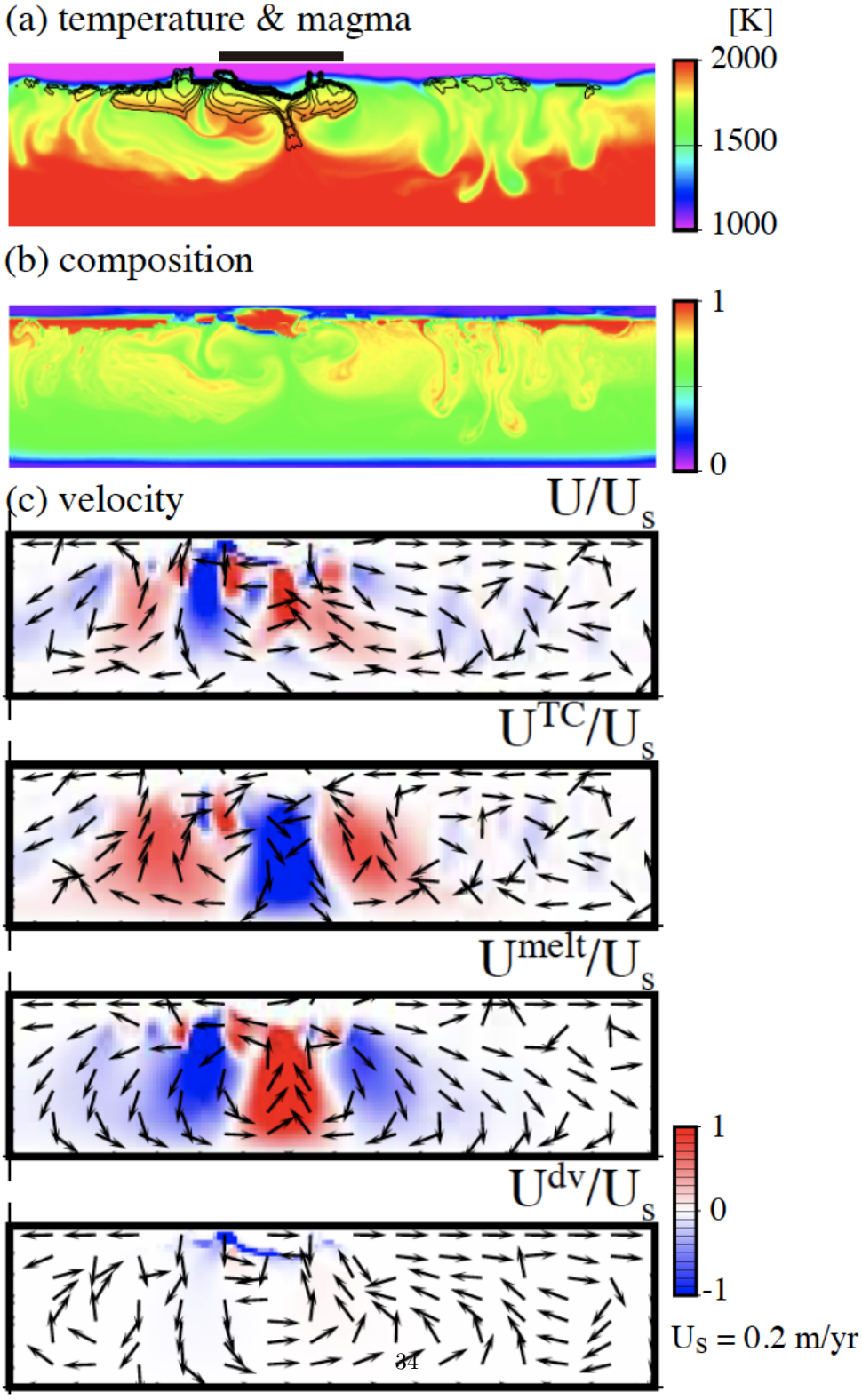
(a) temperature & magma
[K]
2000
1500
1000
(b) composition
1
0
(c) velocity
U/U_s
U^TC/U_s
U^melt/U_s
U^dv/U_s
1
0
-1
U_S = 0.2 m/yr

Figure 5. The same as Figure 4 but for the frame of 0.629 Gyr in Figure 2.

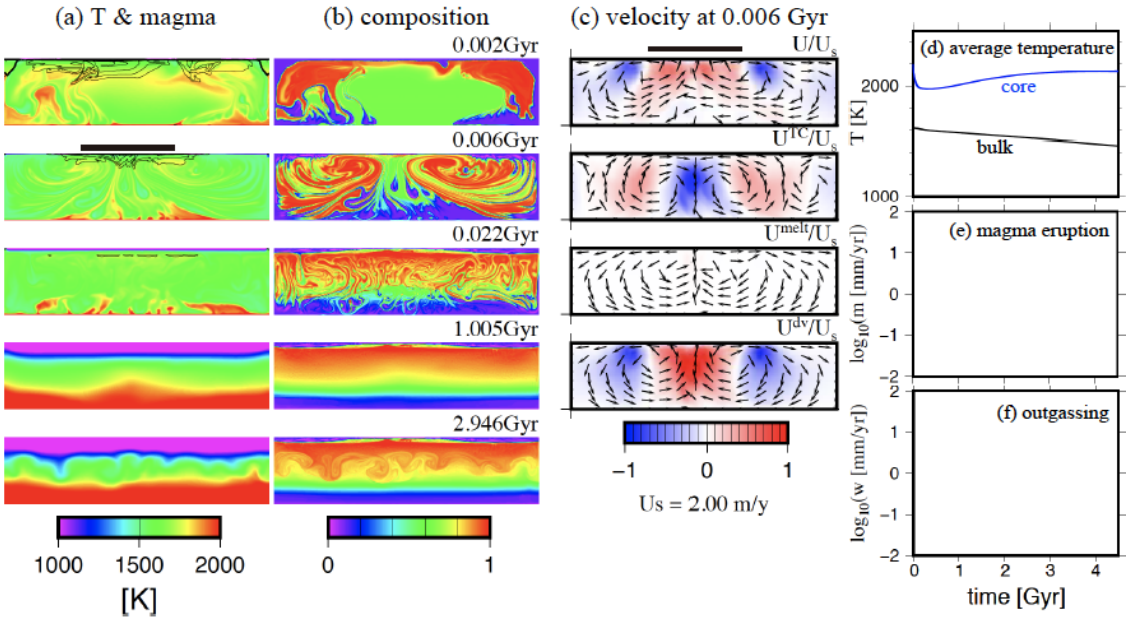

Figure 6. (a) to (c) The same as Figure 4, but for Case H16-050i where the reference permeability Pm is 10 times as high as that of the reference case presented in Figures 2 to 5. Also presented are (d) the average temperature in the box (bulk) and the core, (e) the average eruption rate of magma, and (f) the average outgassing rate, all plotted against time.

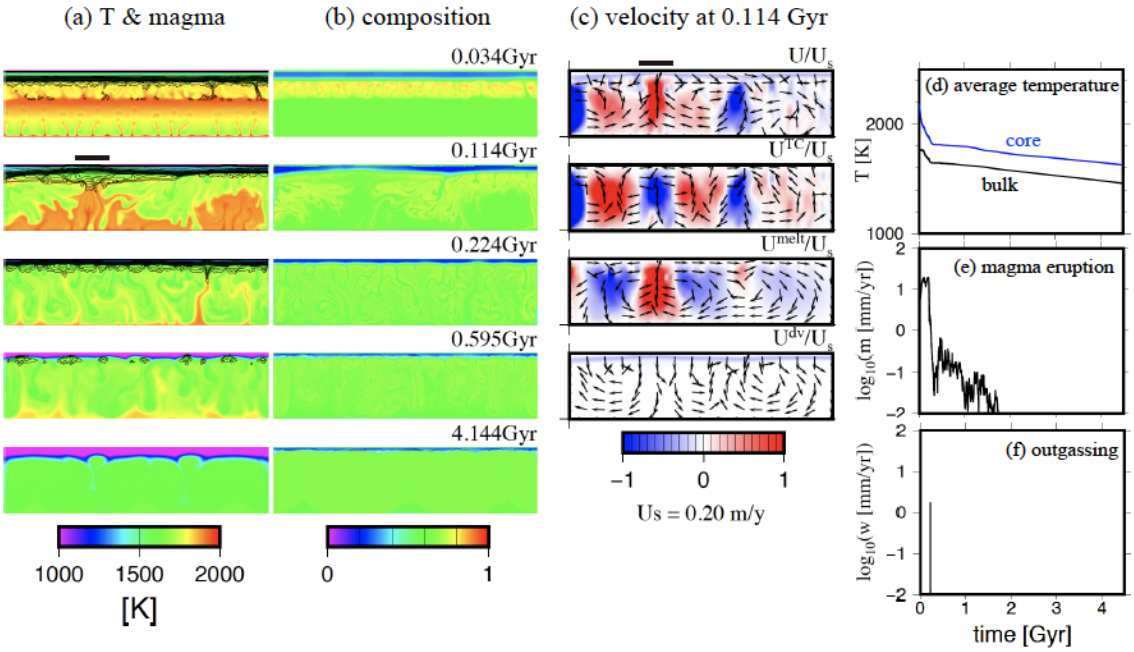

Figure 7. The same as Figure 6, but for Case H16-050j where the reference permeability Pm is 1/10 of that of the reference case.

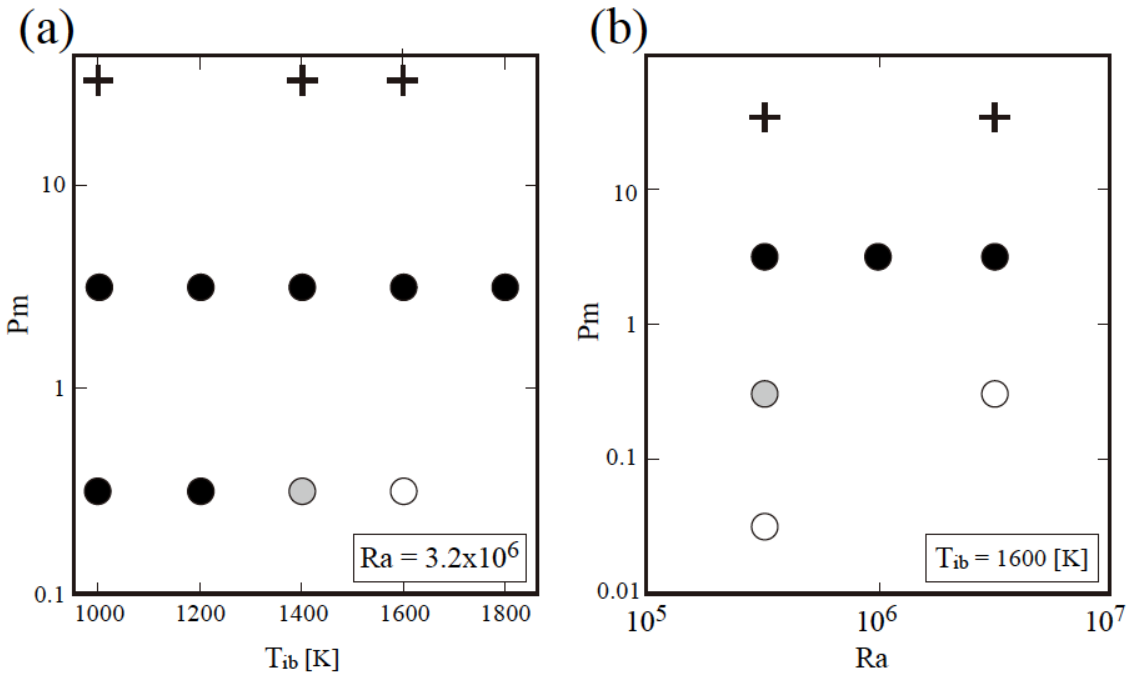

Figure 8. The solid circles show the values of the reference permeability Pm and (a) the initial temperature at the base of the mantle $T_{\rm ib}$ or (b) the Rayleigh number Ra for the cases where the mantle evolves in the four stages shown in Figure 2. The crosses imply that Stage III does not arise (see Figure 6), while the open circles imply that Stage II does not arise (see Figure 7); the gray circles imply that Stage II arises only marginally. All the cases plotted here are calculated at $\phi_w^{\rm init} = 500\ ppm$ and the default values of the parameters E to M listed in Table 2.

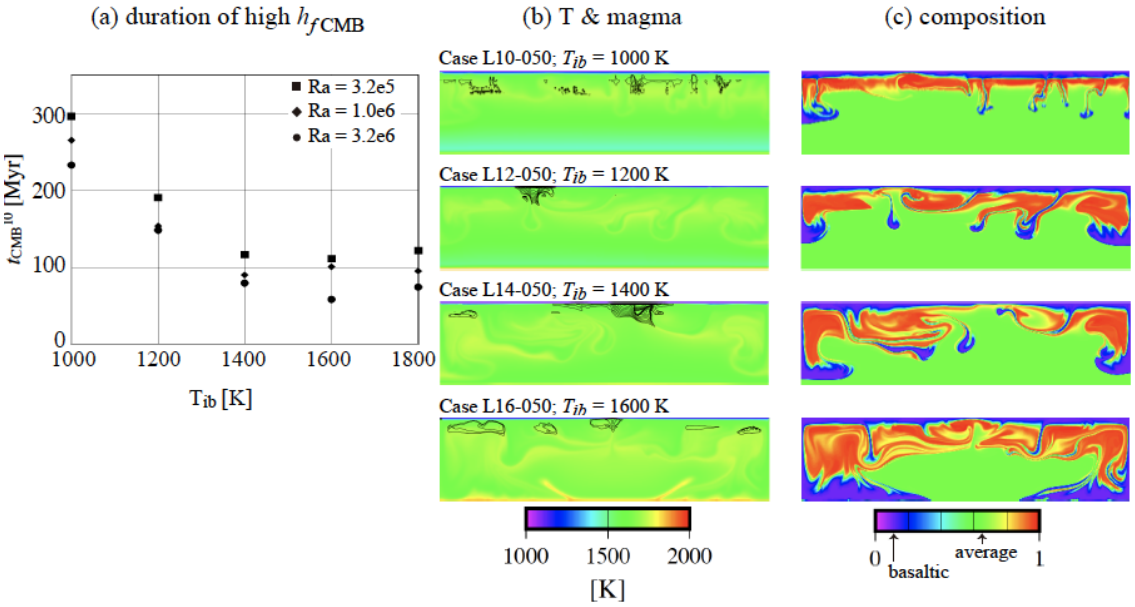

Figure 9. (a) The time $t_{\rm CMB}^{10}$ at which the heat flow on the CMB declines below 10 $mW\ m^{-2}$ plotted against the initial temperature at the base of the mantle $T_{\rm ib}$ for the cases where $\phi_w^{\rm init} = 500\ ppm$ and the default values of parameters listed in Table 2 are assumed. (b), (c) Snapshots of the distributions of temperature, magma, and composition taken at the end of Stage I for the cases indicated by solid squares in (a).

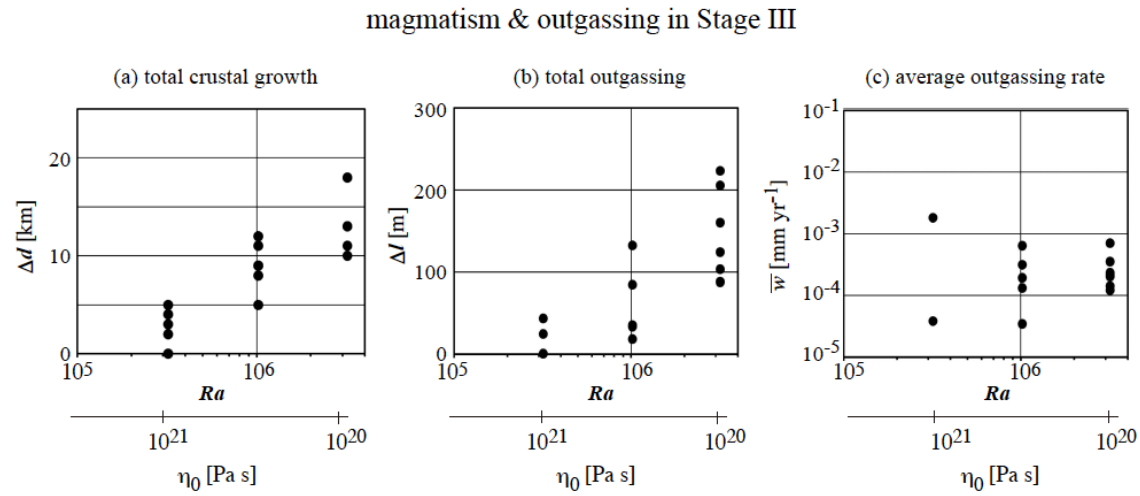

Figure 10. The total amount of (a) crustal growth Δd and (b) water-outgassing Δl in Stage III plotted against the Rayleigh number Ra for the cases where

$Pm = 3.2$, $\phi_W^{\rm init} = 250,\ 500\ ppm$, and the default parameter values of Table 2 are assumed. $T_{\rm ib}$ is in the rage of 1000-1800 K. Δd and Δl are measured in the unit of global equivalent layer (GEL) thickness. Also presented is (c) the plot of the average outgassing rate $\overline{w}$ defined by Equation (12) versus Ra. The value of the reference mantle viscosity η_0 that corresponds to Ra is shown at the base of the plots, too.

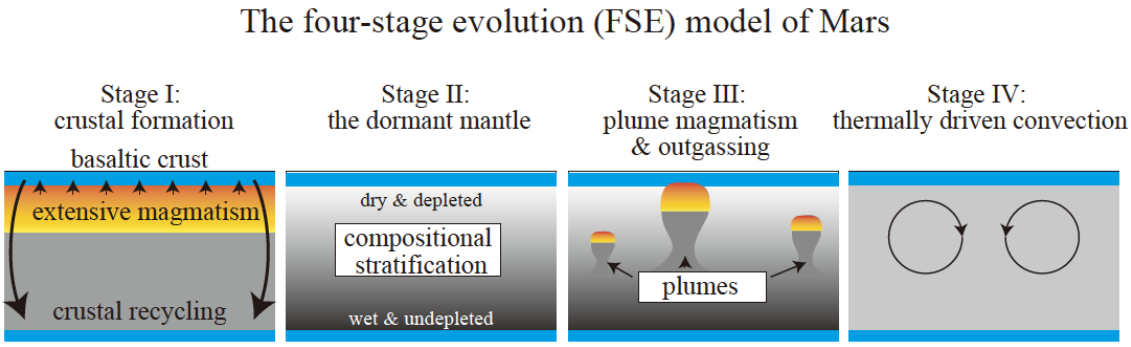

Figure 11. An illustration of the four-stage evolution model of the mantle. The yellow color stands for melting.

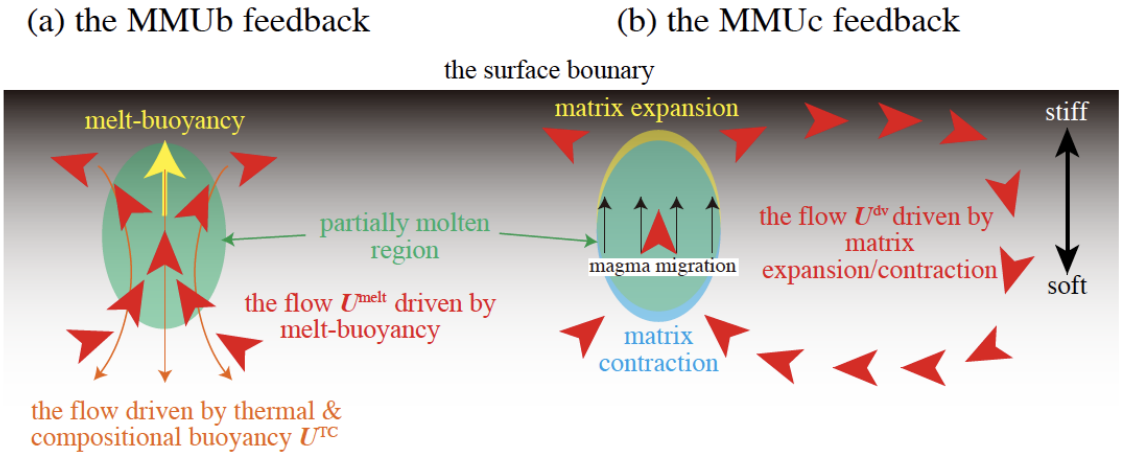

Figure B1. An illustration of the (a) MMUb and (b) MMUc feedback, reproduced from *Ogawa* [2020].